

Structural Characterization of Model Gels under Preparation Conditions and at Swelling Equilibrium

R. Scholz[†] and M. Lang^{*,†}Cite This: <https://doi.org/10.1021/acs.macromol.3c02607>

Read Online

ACCESS |



Metrics & More

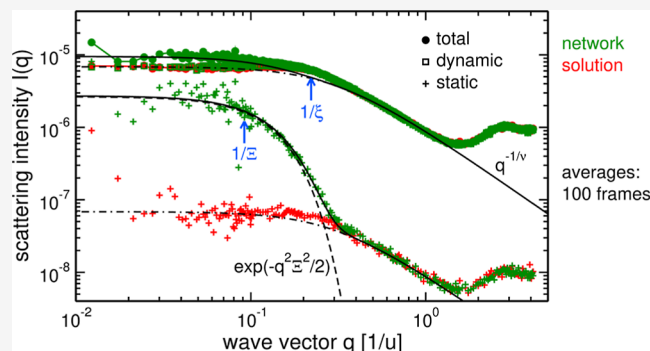


Article Recommendations



Supporting Information

ABSTRACT: We use large-scale computer simulations of star polymer gels to analyze which structural features can be assessed from scattering data of polymer networks. We separate static and dynamic contributions of the scattering intensity $I(q)$, allowing us to determine the correlation length ξ of the corresponding polymer solution and the static correlation length Ξ of network inhomogeneities, combining several properties of the denser cross-link blobs. The dynamic contribution I_{dyn} is related to the correlation length ξ , incorporating parts of the form factor of the star polymer for polymer volume fractions around the overlap condition. At swelling equilibrium, the cross-link motion is confined within a volume comparable to the size of the somewhat denser cross-link blob. Since the cross-link blob size scales $\propto \xi$, we measure $\Xi \propto \xi$ for our nearly ideal model networks. The motion of the cross-links in a harmonic confining potential implies a Gaussian shape of the static density inhomogeneities, a dependence confirmed by the static contribution to the scattering data of all samples in our study. At swelling equilibrium, dynamic scattering $I_{\text{dyn}}(0)$ from thermal fluctuations is almost identical to the scattering intensity $I_{\text{stat}}(0)$ from static inhomogeneities. At preparation conditions, $I_{\text{stat}}(0)/I_{\text{dyn}}(0)$ decays with a power law following the polymer fraction of the cross-link blobs. Here, the larger volume available for cross-link motion stands out for increasing polymer volume fraction ϕ , reducing the concentration dependence of Ξ .



1. INTRODUCTION

Polymer networks and gels have the ability to adjust the volume when exposed to a suitable solvent, resulting in significant changes of gel volume and material properties, like permeability or resistance to mechanical deformations. The relevance of this behavior is highlighted in numerous technical applications operating at swelling equilibrium or utilizing the swelling process. Examples include tissue engineering and other biomedical applications,¹ antimicrobial hydrogels,² wearable sensing, soft robotics,³ drug delivery systems,⁴ soft contact lenses,⁵ food science,⁶ or superabsorbent materials,⁷ among many others.⁸

The key to tailor the properties of the networks and gels is to understand the structure of the material on the relevant length scales. This task inevitably requires reliable tools for analyzing and interpreting the structure of these materials. In this respect, well-defined model systems are highly valuable for developing and testing theoretical predictions. Decades ago, the end-linking of linear chains by multivalent junctions was considered to be the best way for producing the required model networks.^{9–12} To date, comparison with end-linked model networks still pushes our understanding of network structure¹³ and rubber elasticity^{14–18} to new limits.

More recently, it has been shown that a cross-coupling scheme of monodisperse 4-arm star polymers¹⁹ produces

networks with superior material properties as compared to end-linked model systems,²⁰ mainly due to avoiding pending loop defects.^{21,22} At present, these star polymer networks are considered as an ideal model system to improve our understanding of the properties of polymer networks,²³ and they are frequently used for developing and testing theory.^{24–27} The ideality of these samples is also advantageous for understanding scattering experiments because they produce very little excess scattering^{28–30} when compared with a polymer solution at the same polymer volume fraction and composition.³¹ Similar trends for regular networks are observed only in the limit of long elastic strands significantly exceeding the entanglement length³² and when linking the arm ends of star polymers by a bifunctional unit.³³ Hence, the improved homogeneity largely simplifies the analysis of the generic structural features of star polymer model networks.

Received: December 19, 2023

Revised: January 31, 2024

Accepted: February 7, 2024

Scattering techniques are the basic tool to analyze the structure of polymer gels and networks.^{34–37} The major challenge for understanding experimental data arises from the fact that scattering experiments on isotropic samples provide “only” the Fourier transform of the radial pair correlation function instead of the full description of a 3-dimensional structure. Hence, the significant data reduction along this path can produce rather similar results for quite different structures.^a For a deeper insight into the network structure, labeling was used to mark individual chains,^{38–44} linear chains spanning several network strands,^{45–52} or the regions around the network junctions,^{38,53} see Figure 1 for an illustration.

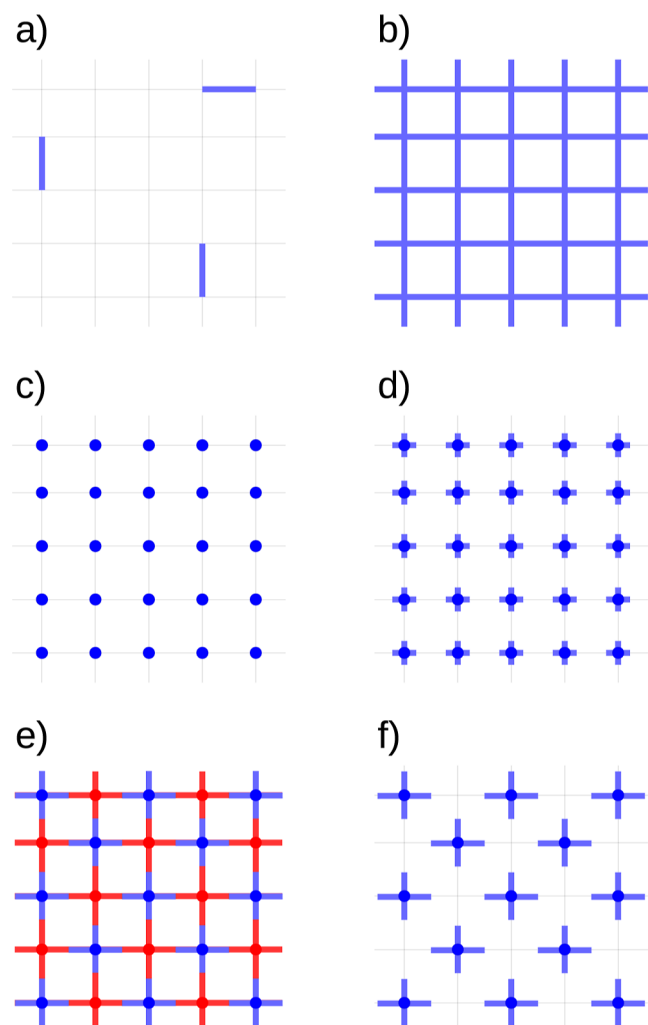


Figure 1. Different ways to label polymer networks: (a) single chains, (b) full polymer network, (c) only cross-links, and (d) chain ends or small regions around cross-links. In heterocomplementarily coupled conetworks of star polymers, either both stars can (e) have maximum contrast or (f) only one type of star is labeled.

Besides these classical ways to label parts of the network, the cross-coupling scheme of Sakai¹⁹ provides the possibility to address the scattering of conetworks made from star polymers in an idealized way.²¹

The labeling of individual chains (Figure 1a) provides information on the conformations and the deformation behavior of the network chains, while labeling of chain sections longer or shorter than a network chain shifts the analysis to the behavior on the length scale of the

corresponding sections. Scattering data of single chains (Figure 1a) have been discussed recently⁵⁴ and will not be covered in the present work. If the full network is labeled (Figure 1b), the structural information is limited to the correlation length ξ and static contributions including any kind of a possible heterogeneous sample density on length scales exceeding ξ . In the present work, we use star polymer networks to focus on the generic information, suppressing additional large-scale heterogeneities. Moreover, our simulations provide real-space information on the corresponding structures, allowing for a direct identification of the contributions to the scattering intensity. If only cross-links are labeled (Figure 1c), we expect information about the effective repulsion between the network junctions,⁵⁵ while labels around cross-links (Figure 1d) should provide a mixed information on cross-link repulsion and the form factor of the resulting labeled regions around the junctions. Notably, some works report data for this kind of labeling differing from theoretical predictions or lacking a simple interpretation.^{38,53} We contribute a discussion of (c) and (d) in a subsequent paper.⁵⁶ Finally, a labeling in the form of (e) and (f) is possible with the star polymer network architecture developed by Sakai et al.¹⁹ We discuss these cases in combination with a selective swelling response of the different star polymers in another follow-up work.⁵⁷

In several preceding simulation studies on model gels or (swollen) polymer networks, scattering functions were computed for the full network structure,^{21,58,59} labeled chains,⁶⁰ labeled star polymers,²¹ labels on chain ends,⁶¹ labeled cross-links,^{61,62} and related model systems.^{63–65} However, to date, a systematic discussion of approaches allowing for a data analysis both in real space and regarding scattering data is still lacking, together with a comparison of advantages and limitations of a real space picture and interpretations relying exclusively on the scattering data. With the present publications, we close this gap for completely labeled networks, while the remaining cases of Figure 1 will be addressed in subsequent works.

The simulations and details of the network parameters used in the present and subsequent studies are summarized in Section 2. A set of suitable model functions and their Fourier transforms for interpreting both the real-space structure and scattering data are discussed in Section 3. Our results for the completely labeled networks are presented in Section 4, where we address a decomposition of scattering into contributions from the time-average inhomogeneous density and from time-dependent thermal fluctuations around this average. This decomposition is made both for the preparation state and for swelling equilibrium, providing in each case two correlation lengths ξ and Ξ , where ξ characterizes the solution-like dynamic scattering from thermal density fluctuations and Ξ the network-like static component of the scattering intensity, respectively. While ξ is discussed in depth in Section 4, an explanation for the static correlation length Ξ is developed in Section 5. The key findings of the present study are discussed in Section 6 in the context of preceding literature. Additional information on data averaging and processing, a table with the key results of the simulations, snapshots of the samples, and additional information on the network structure are provided in the Supporting Information.

2. SIMULATIONS

We apply the bond fluctuation model (BFM)^{66,67} to simulate network formation and subsequent structuring of the samples

by a selective solvent. All simulations discussed rely on the LeMonADE implementation^{68,69} of the BFM model on graphical processing units. In the present investigation, we use the simulation data of a preceding paper,²⁵ and we refer the reader to this work for details on the network parameters, sample preparation, equilibration, and the acquisition of conformation data.

In brief, our simulations concern networks where two batches of star polymers were reacted using a cross-complementary coupling scheme, allowing stars of type A to form bonds only with stars of type B. Both batches of stars are monodisperse, with degrees of polymerization $N_A = 37, 73,$ and 145 and $N_B = 53, 97,$ and 181 , originally designed to provide a match with experimental data.⁷⁰ All stars have $f = 4$ monodisperse arms, containing either $(N_A - 1)/f$ or $(N_B - 1)/f$ monomers per arm. Three classes of networks are prepared, where either stars with the smallest, the second largest, and the largest degree of polymerization are reacted, leading to network strands containing $N = 23, 43,$ and 82 segments, respectively. M_A and M_B are the number of star polymers of either type, providing a total of $n = N_A M_A + N_B M_B$ monomers. We study stoichiometric systems where $M_A = M_B$, with a total number of stars $M = 2M_A$. Networks with the three available strand lengths N are prepared from equilibrated polymer solutions over a large range of different polymer volume fractions at preparation, ϕ_0 . Boundary effects are corrected by replacing the nominal volume fraction ϕ_0 by an effective volume fraction ϕ_1 introduced previously.²⁵ In the present work, we analyze 21 out of the 38 networks of this preceding paper. The networks were selected regarding the following three criteria: (a) the samples were prepared in the largest box (size $L = 512u$, where u is the lattice constant) to minimize finite size effects and to maximize the available range of the scattering vector \mathbf{q} , (b) ϕ_0 must be sufficiently low to allow for an unambiguous determination of ξ in the preparation state, and (c) ϕ_0 must be sufficiently large to see sufficient volume change upon swelling. The results for all networks are summarized in Table S1 of the [Supporting Information](#); key features of the networks are found in Table 1 of ref 25 by comparing with data for the same $N, M,$ and L . As described in ref 70, the concentration scale was matched with the experiments, setting a reference value for the overlap polymer volume fraction ϕ^* of the star polymers. We use this reference in the present work by presenting the data as a function of ϕ^* for a rough orientation. The conversion of all samples is identical, $p = 0.95$, eliminating additional dependencies of p on the polymer volume fraction ϕ in the samples. Additionally, we prepared networks in periodic boundaries with the same parameters as the networks in the nonperiodic boxes for testing the impact of the confining wall on the simulation results.

3. STRUCTURAL ANALYSIS OF THE NETWORKS

In the present section, we compile several definitions and model equations that are used in the present work for the characterization of the network structure. These equations focus on basic relations used to compute the scattering intensity or pair correlation of the samples, and on particular models for either pair correlation or scattering data.

3.1. Scattering Intensity. For each snapshot, the scattering intensity $I(\mathbf{q})$ is calculated from a Fourier transform of the monomer positions, allowing for a discrete set of wave vectors \mathbf{q} on the lattice, with

$$\mathbf{q} = \frac{2\pi}{L}(j_x, j_y, j_z) \quad (1)$$

where $L = lu$ is the size of the cubic box, and $0 \leq j_x, j_y, j_z < l$ are integers. The scattering intensity is given by

$$I(\mathbf{q}) = \langle |\sum_{j=1}^n a_j e^{i\mathbf{q}\cdot\mathbf{r}_j}|^2 \rangle \quad (2)$$

where \mathbf{r}_j is the position of monomer j , a_j describes its scattering length, and $\langle \dots \rangle$ denotes an ensemble average over independent configurations of the same network. We use $n_A = M_A N_A$ and $n_B = M_B N_B$ to denote the total numbers of A and B monomers, respectively. We arrange all monomers such that the first n_A monomers are of type A, and we assume that the scattering lengths depend only on the type of monomer. This gives

$$I(\mathbf{q}) = \langle |a_A \sum_{j=1}^{n_A} e^{i\mathbf{q}\cdot\mathbf{r}_j} + a_B \sum_{k=n_A+1}^{n_A+n_B} e^{i\mathbf{q}\cdot\mathbf{r}_k}|^2 \rangle \quad (3)$$

Different choices of the scattering lengths give access to complementary observables. The most natural choice consists in equal amplitudes for all monomers, $a_A = a_B = 1/(n_A + n_B)$, which we abbreviate as $I_{\text{all}}(\mathbf{q})$ in the following, corresponding to the situation in [Figure 1b](#). For the choice $a_A = 1/n_A$ and $a_B = 0$, we obtain the normalized scattering intensity $I_{AA}(\mathbf{q})$ among monomers of type A, and for $a_A = 0$ and $a_B = 1/n_B$, we get the normalized scattering intensity $I_{BB}(\mathbf{q})$ among B monomers ([Figure 1f](#)). For $a_A = 1/(2n_A)$ and $a_B = 1/(2n_B)$, a “non-selective scattering” intensity is obtained, where all stars contribute with the same weight, which we call $I_{A+B}(\mathbf{q})$. Moreover, the maximum contrast between A and B polymers ([Figure 1e](#)) can be calculated with $a_A = 1/(2n_A)$ and $a_B = -1/(2n_B)$, resulting in a scattering intensity abbreviated as $I_{A-B}(\mathbf{q})$. Experimentally, such a maximized contrast in small-angle neutron scattering data can be achieved via synthesis of the precursor stars from materials with controlled deuteration. In general, in simulations, arbitrary choices of labeled monomers of “type A” against unlabeled monomers of “type B” can be made, allowing us to treat any kind of labeling in a similar manner, including the cases illustrated in [Figure 1c,d](#).

Using the above conventions for the scattering length, the first four cases are normalized to $I_{\text{all}}(0) = I_{AA}(0) = I_{BB}(0) = I_{A+B}(0) = 1$ for a zero wave vector, while the scattering intensity with maximum contrast vanishes for $\mathbf{q} = 0$, i.e., $I_{A-B}(0) = 0$. In the figures presented below, scattering intensities obtained for the same absolute of the wave vector $q = |\mathbf{q}|$ are averaged isotropically, resulting in $I(q)$. Data averaging for all plots containing scattering intensities from simulations was performed as described in the [Supporting Information](#).

3.2. Pair Correlation Functions. In order to allow for a more detailed interpretation of the arrangement of the monomers or the segregation between A and B components in real space, we introduce several pair correlations (also called “pair distribution functions”) between different types of monomers. For an extended homogeneous system involving n_A A monomers and n_B B monomers within a reference volume V , these pair correlations shall converge to a limit of 1 for large distances. Accordingly, they can be defined by counting the number of pairs within a shell of thickness Δr around a distance r , e.g., for A–A pairs

$$g_{AA}(r) = \frac{V}{n_A^2 4\pi r^2 \Delta r} \sum_{j=1}^{n_A} \sum_{k=1}^{n_A} \Theta \left[\frac{\Delta r}{2} - |(|r_j - r_k| - r)| \right] \quad (4)$$

where Θ is the Heaviside step function that is equal to 1 in the interval $r - \frac{\Delta r}{2} < |r_j - r_k| < r + \frac{\Delta r}{2}$ and 0 outside this interval. Other quantities like $g_{AB}(r)$ and $g_{BB}(r)$ or the pair correlation function of the full network, $g_{all}(r)$, can be defined similarly. In a macroscopic experiment, the above pair correlations $g_{AA}(r)$, $g_{AB}(r)$, and $g_{BB}(r)$ converge to a constant value of 1 for large radii, as the sample size is typically huge as compared to the structure that is analyzed. We reproduce this behavior in simulations of the as-prepared state with periodic boundary conditions. The pair correlation with maximum contrast among both types of polymers can be defined as

$$g_{A-B}(r) = \frac{1}{4} [g_{AA}(r) - 2g_{AB}(r) + g_{BB}(r)] \quad (5)$$

From these radial pair correlations, we obtain the respective scattering intensities via a radial sine Fourier transform, using

$$I_{AA}(q) \propto \int_0^\infty dr 4\pi r^2 [g_{AA}(r) - 1] \frac{\sin(qr)}{qr} \quad (6)$$

for the pair correlations with a long distance limit of unity like $g_{AA}(r)$, $g_{BB}(r)$, $g_{A+B}(r)$, and $g_{all}(r)$. Among these, the limit $q \rightarrow 0$ of $I_{all}(q)$ is inversely related to the osmotic compressibility of the system, $I(q) \propto [d\Pi(c)/dc]^{-1}$.⁷¹ For the pair correlation $g_{A-B}(r)$ with vanishing long distance limit, see Figure 1e; we use the transform

$$I_{A-B}(q) \propto \int_0^\infty dr 4\pi r^2 g_{A-B}(r) \frac{\sin(qr)}{qr} \quad (7)$$

3.3. Data Analysis of Homogeneous Samples. In what follows, we introduce different indices to distinguish model functions adapted to specific situations. These contain the Debye function (D) for ideal chains, the Ornstein–Zernike function (OZ),⁷² and its generalization to fractals (F)⁷³ for polymer solutions or networks. Sample inhomogeneities will be modeled as hard spheres (HS) by the Debye–Bueche model (DB)⁷⁴ or by Gaussian distributions (G). Where possible, closed analytical forms will be given both for scattering intensities $I(q)$ and for pair correlations $g(r)$.

An ideal chain in a dense melt or in a dry network (Figure 1a) scatters according to its form factor described by the Debye function

$$I_D(q) = \frac{2}{O^2} [\exp(-O) - 1 + O] \quad (8)$$

with $O = q^2 R_g^2$ allowing us to extract the squared radius of gyration of the chain from the data, whereas the collective behavior of the entire sample (Figure 1b) can be modeled by an Ornstein–Zernike function

$$I_{OZ}(q) \propto \frac{1}{1 + (q\xi)^2} \quad (9)$$

compatible with an exponentially decaying pair correlation, $g(r) - 1 \propto e^{-r/\xi}/r$.

In a system with fractal dimension $D_f = 1/\nu$ over the distance range $b \leq r \leq \xi$ between monomer size b and correlation length ξ , the number of monomers within a range r scales as $N(r) \propto r^{D_f}$. Moreover, assuming that the deviation of

the radial pair correlation from its asymptotic limit toward large distances decays exponentially as $e^{-r/\xi}$, the integrand in a radial Fourier transform like eq 6 becomes proportional to

$$g(r) - 1 \propto r^{D_f-3} e^{-r/\xi} \quad (10)$$

The resulting scattering intensity can be obtained analytically^{73,75,76}

$$I_F(q) = \frac{1}{(1 + q^2 \xi^2)^{(D_f-1)/2}} \frac{\sin[(D_f - 1) \arctan(q\xi)]}{(D_f - 1)q\xi} \quad (11)$$

normalized here to $I_F(0) = 1$. Please note that the fractal exponent D_f determined from fitting the asymptotic dependence of the scattering intensity at large q via the above definition of $I_F(q)$ will differ from an analysis relying on alternative approximations like $I(q) \propto 1/(1 + q^2 \xi^2)^{D_f/2}$ or $I(q) \propto 1/(q\xi)^{D_f}$. Equation 11 has been applied successfully to scattering data from fractal silica aggregates,⁷⁷ protein complexes,⁷⁸ and swollen polymer networks.⁷⁹ For a swollen polymer phase in an a-thermal solvent, we expect $\nu \approx 0.5876$ ⁸⁰ and $D_f = 1/\nu \approx 1.70$. Among different possible model functions with asymptotic decay $\propto q^{-1/\nu}$,^{81,82} eq 11 has the advantage of relying on an analytic model for $g(r)$. Moreover, a Taylor series expansion up to the order $q^2 \xi^2$

$$I_F(q) \approx 1 - \left[\frac{1}{3} + \frac{D_f - 1}{2} + \frac{(D_f - 1)^2}{6} \right] q^2 \xi^2 \quad (12)$$

$$\approx \frac{1}{1 + \left[\frac{1}{3} + \frac{D_f - 1}{2} + \frac{(D_f - 1)^2}{6} \right] q^2 \xi^2} \quad (13)$$

can easily be compared to other known model functions like $I_D(q)$ or its Taylor series expansion. For simplicity, we restrict this comparison to the reference case of ideal chains, $D_f = 2$, and we use a notation where the second order of the Taylor series is moved to the denominator, guaranteeing a decrease toward large q . Then, both the Guinier approximation for the form factor and the Debye function give

$$P(q) \approx \exp\left(-\frac{q^2 R_g^2}{3}\right) \approx \frac{1}{1 + \frac{q^2 R_g^2}{3}} = \frac{1}{1 + \frac{q^2 R_c^2}{18}} \quad (14)$$

so that we recognize that the real space end-to-end distance of a correlated chain section as expressed by R_c is larger than ξ by a factor of roughly $R_c/\xi \approx \sqrt{18} \approx 4.24$.

3.4. Boundary Effects and Frozen Inhomogeneities.

In finite samples, all pair correlations inside the network converge to zero at distances exceeding the size of the sample, and therefore, we have to correct for the shape of the network. As a rough approximation, the nearly cubic shape of our aperiodic polymer slabs can be captured by the behavior of a HS with radius R

$$g_{HS}(r, R) = \left[1 - \frac{3}{4} \left(\frac{r}{R} \right) + \frac{1}{16} \left(\frac{r}{R} \right)^3 \right] \quad (15)$$

Hence, the scattering intensities of a finite size sample will roughly resemble the form factor of a HS^{83,84}

$$P_{HS}(q, R) = \left(\frac{3}{(qR)^3} [\sin(qR) - qR \cos(qR)] \right)^2 \quad (16)$$

normalized here to $P_{\text{HS}}(0) = 1$. Taking the cubic shape into account, the Fourier transform over the finite box size along each Cartesian direction will result in pronounced spikes at wave vectors parallel to a Cartesian direction like $q = \frac{2\pi}{L}(j_x, 0, 0)$, with intensities scaling as $1/j_x^2$. As demonstrated below, the interpretation of scattering data from aperiodic polymer slabs becomes simpler when ignoring the respective discrete values of q : periodic and aperiodic samples at otherwise equivalent preparation conditions show matching scattering data at all absolute values of wave vectors $q = |q|$ where contributions along Cartesian directions do not dominate.

Alternatively, sample inhomogeneities fading away over a large length scale can be modeled by an exponentially decaying contribution to the radial pair correlation function as proposed by Debye and Bueche⁷⁴

$$g_{\text{DB}}(r) \propto e^{-r/\xi_{\text{DB}}} \quad (17)$$

compatible with a contribution to scattering intensity

$$I_{\text{DB}}(q) \propto \frac{1}{[1 + (q\xi_{\text{DB}})^2]^2} \quad (18)$$

The scattering intensities according to eqs 16 and 18 decay $\propto 1/q^4$ for large wave vectors, in accordance with Porod's law for sharp boundaries.

By a combination of dynamic and static scattering techniques, a static, "frozen", and nonergodic density heterogeneity can be separated from a contribution that is homogeneous, ergodic, and dynamic.^{36,85,86} In simulations, the frozen density inhomogeneity is available from the time average of the density at each lattice site of the simulation box. A simple model for randomly dispersed static domains on top of a homogeneous medium consists of a Gaussian pair distribution proportional to

$$g_{\text{G}}(r) \propto \exp\left(-\frac{r^2}{2\xi^2}\right) \quad (19)$$

transforming into a contribution to scattering with Gaussian shape

$$I_{\text{G}}(q) \propto \exp\left(-\frac{q^2\xi^2}{2}\right) \quad (20)$$

For rather inhomogeneous polymer networks, the resulting scattering intensity may dominate the measured data over a certain range of wave vectors $q < 1/\xi$, and accordingly, fits of scattering data allowing for a combination of eqs 9 and 20 can reveal both ξ and $\Xi \gg \xi$,^{87,89} whereas a linear combination of eqs 9 and 18 may be used as an alternative interpolation of measured data.⁸⁸

3.5. Structure at Small Length Scales. At larger wave vectors, small interatomic distances between adjacent molecules result in further scattering peaks, best documented for pure solvents, where they can be related to the structure factor of the liquid and to the respective pair correlation.^{90,91} In our simulations, we either use implicit solvent or we assign a scattering amplitude of zero to an explicit solvent. Therefore, scattering peaks at large q correspond to the packing of the nearest neighboring monomers on the lattice. These contributions are discarded by restricting fits of simulated scattering data to $q < 1/u$.

3.6. Scaling of Simulated Scattering Intensities. At $q = 0$, according to eq 3, all monomers in the system interfere constructively with phase factors of unity. With our conventions for the scattering amplitudes introduced above, the resulting scattering intensities are normalized to one, e.g. $I_{\text{all}}(0) = 1$. When analyzing the shape of the simulated scattering intensity in the limit $q \rightarrow 0$ with some model function, e.g., $I_{\text{F}}(q)$, the amplitude of this model function measures the fraction of all monomers still interfering constructively. In a solution of long linear polymers, this corresponds to the number of monomers in a correlation volume divided by the total number of monomers in the system. In a polymer network, such a contribution can be superimposed with the excess scattering around the cross-links as discussed in the following sections.

4. RESULTS

An advantage of computer simulations is that real space information including the full network connectivity can directly be compared with the scattering data of the samples. Moreover, the scattering data can be decomposed into a static and a dynamic contribution by considering either time average or instantaneous particle densities. Finally, we can track the swelling of particular locations inside the network and correlate these with features of the network structure. The combination of these possibilities is particularly interesting for testing different models regarding the swelling of networks and the excess scattering of the networks as compared to a polymer solution at the same polymer concentration. This testing is performed against the simulation data of heterocomplementarily coupled star polymer model networks that are the current "gold standard" for homogeneous networks. In this way, we can identify the generic contributions to the scattering signal of polymer networks and gels aside from additional contributions that encode heterogeneity on large length scales.

4.1. Scattering Data at Preparation Conditions. The scattering intensities $I_{\text{all}}(q)$ of a series of star networks and star solutions prepared at different polymer volume fractions were calculated according to eq 3, see Figure 2. In simulations of networks in a periodic box, fits with a model function for a fractal dimension $D_{\text{f}} = 1/\nu$ according to eq 11 for $\nu = 0.5876$ ⁸⁰ are suitable for a smooth interpolation of the numerical data for all $q < 1/u$. The results for the correlation length are given in Table S1 of the Supporting Information as ξ_{all} . Scattering data in an aperiodic simulation box agree with these data when spikes at specific wave vectors $q = j(2\pi/L)$ with integer j are omitted. This good correspondence demonstrates that boundary effects have little impact on the structure of the networks, showing that the aperiodic samples are suitable for studying equilibrium swelling. This is corroborated by the close correspondence of the measured correlation lengths of the samples in the preparation state with and without periodic boundary conditions, see Table S1.

In Figure 2, scattering data from star solutions coincide with data from star networks over the region $q > 0.2/u$ for all polymer volume fractions. At lower wave vectors and for small polymer volume fractions $\phi_0 \lesssim \phi^*$, the networks produce significant excess scattering as compared to the solutions, whereas this effect fades out for ϕ_0 significantly above ϕ^* , in agreement with the experiment.^{31,92} Similar to experimental findings, see Figure 4 of ref 93, the structure factor of star polymers ("star hump"⁹⁴) becomes apparent in the solution data around ϕ^* . In the opposite limit of large ϕ_0 , the

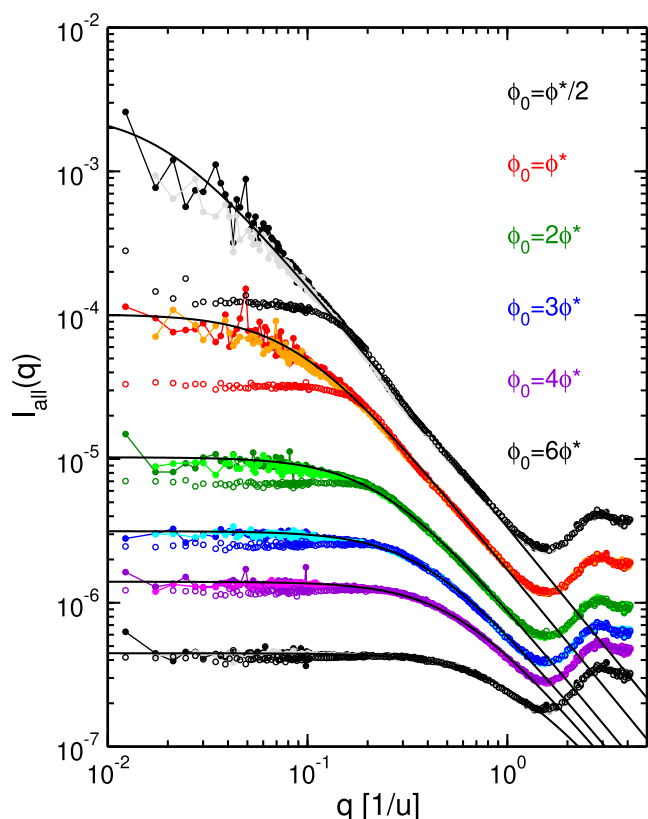


Figure 2. Scattering intensity $I_{\text{all}}(q)$ for periodic networks (dots in darker colors), aperiodic samples (dots in lighter colors), and star solutions (open circles) with star size $N_A = 73$ and $N_B = 97$ in a simulation box $L = 512u$, corresponding to polymers with $N = 43$ segments connecting adjacent star centers. The data of the periodic networks were fit with the model function $I_F(q)$ for fractal dimension $D_f = 1/\nu$ with $\nu = 0.5876$ ⁸⁰ according to eq 11, for $q < 1/u$ (black lines), revealing the correlation length ξ_{all} . Data averaging was performed as described in the Supporting Information.

correlation length ξ_{all} becomes too small to interfere with the characteristic star hump, but there, the intensity decay of the scattering data becomes quite limited, see, e.g., the $6\phi^*$ data in Figure 2. In fact, this prevented us from also analyzing the networks of our preceding paper²⁵ prepared in simulation containers with $L = 256u$ and referring to larger ϕ_0 than shown in Figure 2. Moreover, the decreasing dynamic range of $I_{\text{all}}(q)$ for large ϕ_0 inhibits a stable determination of ν from a fit to the data, whereas at small ϕ_0 , close agreement with the theoretical prediction was achieved. Therefore, we have fixed the asymptotic decay of the model function by using $\nu = 0.5876$ ⁸⁰ throughout.

A more detailed analysis of the scattering data is possible when splitting the data into a static and a dynamic contribution. This is achieved by computing additional scattering functions from the time-averaged density profiles of the networks.⁵⁸ In more detail, the scattering data as presented in Figure 2 refer to an average of the scattering data summed over $X = 100$ independent frames, corresponding to a time average of the scattering intensity

$$I_{\text{all}}(q) = \langle I_{\text{all}}(q, t) \rangle_t \quad (21)$$

On the other hand, the same $X = 100$ independent frames can be superimposed on the lattice, defining throughout the sample a local time average of the polymer density. This time average

density allows to compute a static contribution to the scattering data, abbreviated as $I_{\text{stat}}(q)$ in the following. On this basis, we can decompose the time average scattering intensity into scattering from static density inhomogeneities and dynamic scattering arising from solution-like thermal fluctuations of the density around its local time average^{85,86}

$$\langle I_{\text{all}}(q, t) \rangle_t = \langle I_{\text{dyn}}(q, t) \rangle_t + I_{\text{stat}}(q) \quad (22)$$

After extracting both $I_{\text{all}}(q)$ and $I_{\text{stat}}(q)$ from the simulations, the dynamic scattering $I_{\text{dyn}}(q, t) = \langle I_{\text{dyn}}(q, t) \rangle_t$ can easily be determined from their difference according to eq 22. The origin of the static intensity $I_{\text{stat}}(q)$ is explored in detail in Section 5.

In a trivial case like a solution of star polymers, no static density inhomogeneities are possible, so that $I_{\text{stat}}(q)$ vanishes for $X \rightarrow \infty$. For a finite set of X frames, $I_{\text{stat}}(q)$ remains finite and reproduces the shape of $I_{\text{all}}(q)$, but with an intensity reduced by a factor $1/X$ if the consecutive frames are independent. This dependence was tested successfully with the data of the star polymer solutions, which can be approximated by a model function $I_F(q)$, see Figure S1 and Section SII of the Supporting Information. Moreover, this test revealed that the time interval between consecutive frames is sufficiently long to provide independent data on all length scales relevant for our analysis. For analyzing the static part of the scattering intensity, we thus assume model functions of the form of $I_G(q) + I_F(q)/X$ according to eqs 11 and 20. As shown in Figure 3, this model function interpolates the data quite well and reproduces the factor of $1/X$ for the high q part of the static contribution, whereas the total intensity $I_{\text{all}}(q)$ is well approximated by $I_G(q) + I_F(q)$. This procedure allows us to separately determine the static correlation length Ξ_0 at preparation conditions from $I_{\text{stat}}(q)$ and the correlation length ξ_0 from $I_{\text{dyn}}(q)$. The resulting fits for the correlation lengths based upon this analysis are summarized in Table S1 of the Supporting Information.

Our fractal model function $I_F(q)$ does not account for Benoit's star hump.⁹⁴ Hence, in order to obtain more reliable estimates for the correlation length ξ , we exclude the region of the star hump from the fit. In effect, the amplitude of $I_F(q)$ is mainly determined within the interval $(0.01/u \leq q \leq 0.05/u)$, whereas a combination with the decay over large wave vectors $(0.6/u \leq q \leq 1/u)$ provides ξ . Figure 3 reveals that this procedure reduces significant deviations between $I_{\text{dyn}}(q)$ and the fit with $I_F(q)$ to the excluded intermediate range $0.05/u \leq q \leq 0.6/u$ where the form factor of the stars produces the expected hump in the numerical scattering data, see also Figure 4 of ref 93 or Figure 5 of ref 95.

Please note that a fit of the total scattering data in Figure 2 with a global shape $I_F(q)$ seems to be quite precise over all wave vectors, but as this analysis does not distinguish between static and dynamic contributions to scattering, we consider the resulting correlation length ξ_{all} to be less trustworthy than the correlation length ξ_0 derived from an appropriate analysis of the dynamic part of the scattering intensity alone.

For polymer solutions, a power law dependence $\xi_{\text{sol}} \propto \phi_0^{-\nu/(3\nu-1)} \propto \phi_0^{-\alpha}$ with $\alpha \approx 0.77$ is expected in the good solvent regime,^{96,97} whereas this turns into $\xi_{\text{sol}} \propto \phi_0^{-1}$ for theta solvents. Both regimes are well supported by experimental data for linear chains.^{98,99} We have tested this dependence for our star polymer solutions, leading to a somewhat larger α , see Figure 4 for the plot and Table 1 for the exponents determined

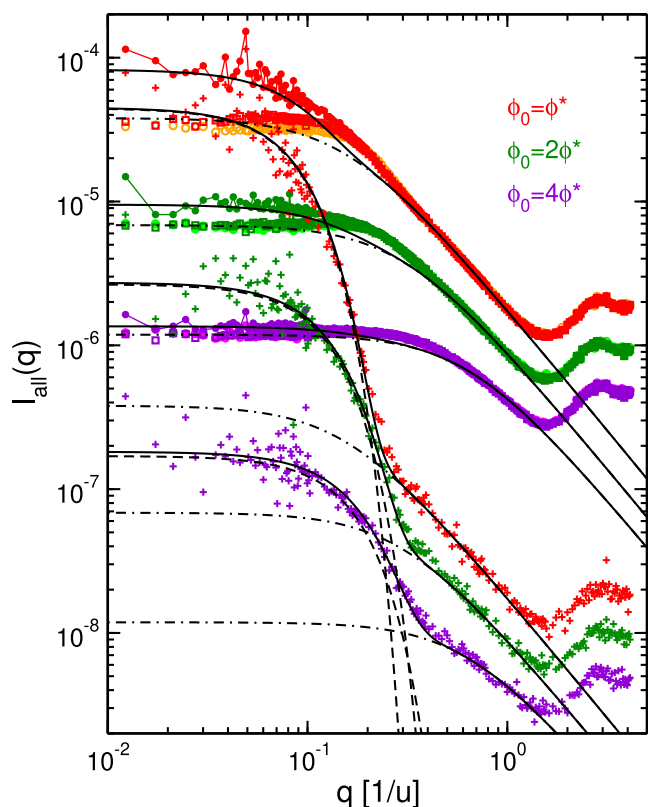


Figure 3. Scattering data from networks with star size $N_A = 73$ and $N_B = 97$ in the preparation state, simulated with periodic boundary conditions in a box $L = 512u$. Symbols with color according to legend: $I_{\text{all}}(q)$ (full dots connected by a line), $I_{\text{stat}}(q)$ (crosses), and $I_{\text{dyn}}(q)$ (open squares). The corresponding scattering intensity $I_{\text{all}}(q)$ from solution is given for comparison [open circles, brighter colors than in the legend]. Fits to $I_{\text{dyn}}(q)$ (dashed-dotted) are performed with $I_{\text{F}}(q)$, eq 11, with $\nu = 0.5876$,⁸⁰ providing ξ_0 . Fits to $I_{\text{stat}}(q)$ (solid lines) are performed with $I_{\text{G}}(q) + I_{\text{F}}(q)/X$ with $X = 100$, relying on eq 20 and the rescaled fit to $I_{\text{dyn}}(q)$ (dashed-dotted), with $I_{\text{G}}(q)$ (dashed) shown separately. The solid lines accompanying $I_{\text{all}}(q)$ represent the sum $I_{\text{G}}(q) + I_{\text{F}}(q)$.

from the entire series of samples. In the fit of ξ_{sol} in Figure 4, we have excluded both the data at the lowest ϕ as it refers to $\phi_0 < \phi^*$ and the data point at the largest ϕ because of the low dynamic range of the scattering data, leading to a correlation length comparable to half the size of a monomer.

For small polymer volume fraction ϕ_0 , in networks with periodic boundaries, we observe a slight enhancement in ξ as compared to ξ_{sol} determined from a star solution, see Figure 4. The trend of a stronger concentration dependence in networks for some ranges of ϕ is also found in refs 100 and 101 where a measured dependence of $\xi \propto \phi_0^{-0.74 \pm 0.01}$ for polymer solutions turns into $\xi \propto \phi_0^{-1.01 \pm 0.07}$ for the corresponding networks. In the experiments on end-linked model networks, this increase carries an additional contribution from inserting the cross-links. In our simulations, we attribute this difference to averaging I_{dyn} over regions with a varying time average density. In contrast to these results for the dynamic correlation length ξ , we obtain a significantly larger exponent α for ξ_{all} in the range of $\alpha \approx 1.3$ for $N = 43$, decreasing significantly with increasing N . Exponents α in a similar range and with the same trend as a function of N were found in experimental studies of star polymer model networks with the same architecture as in our work.^{93,102} A simulation study⁵⁹ with similar parameters as

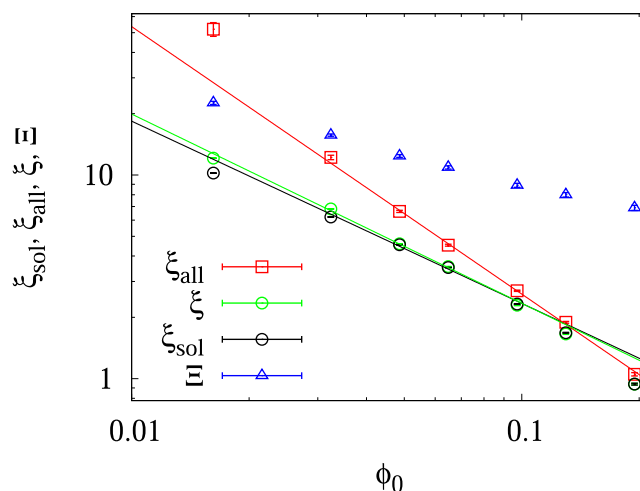


Figure 4. Scaling of correlation length as a function of polymer volume fraction at preparation, ϕ_0 , for a solution consisting of $N_A = 73$ and $N_B = 97$ polymer stars and for the resulting networks in samples with periodic boundaries. The data were fit with power laws $\propto \phi_0^{-\alpha}$, and the resulting exponents α are summarized in Table 1. The static correlation length Ξ is included for comparison. The data points at the lowest $\phi_0 < \phi^*$ and at the highest ϕ_0 with $\xi \approx 1$ were excluded for fitting the scaling of ξ_{all} and of ξ_{sol} , and reasons for restricting the fit interval are given in the text.

Table 1. Scaling Exponents α of Power Laws $\propto \phi^{-\alpha}$, $\phi_0^{-\alpha}$, or $\phi_1^{-\alpha}$, Fitted to the Various Correlation Lengths, for Networks with Different Chain Lengths N Connecting Adjacent Star Centers^a

sample type	N	ξ_{all}	ξ	ξ_{sol}
periodic ϕ_0	23	1.46(3)	0.94(3)	0.77(5)
	43	1.31(3)	0.93(3)	0.90(5)
	82	1.19(3)	0.92(3)	0.85(3)
as prepared ϕ_0	23	1.59(4)	1.01(2)	
	43	1.30(2)	0.96(3)	
	82	1.16(1)	0.90(3)	
as prepared ϕ_1	23	1.97(5)	1.35(4)	
	43	1.41(4)	1.22(4)	
	82	1.29(5)	1.08(2)	
swollen Φ	23	1.8(2)	1.52(5)	
	43	1.56(7)	1.29(2)	
	82	1.3(1)	1.23(4)	

^aThe “periodic” samples were simulated using periodic boundary conditions; all other samples were run in a box with solid walls. For ξ_{sol} and ξ_{all} , the analysis was performed using $I_{\text{all}}(q)$ of either the star polymer solutions or of the networks, at preparation conditions at ϕ_0 or ϕ_1 . In swelling equilibrium, this analysis was performed with $I_{\text{F}}(q) + I_{\text{DB}}(q)$. For determining ξ , the static contribution, $I_{\text{stat}}(q)$, was subtracted from the total signal to provide access to the dynamic contribution, $I_{\text{dyn}}(q)$, following the procedure described in the text.

our data for $N = 43$ arrives at $\xi_{\text{all}} \propto \phi_0^{-1.3}$, closely resembling our results. Experimental data directly demonstrate that ξ_{all} grows during cross-linking, see, e.g., Figure 4 of ref 92. This underlines the fact that ξ_{all} incorporates an increasing static contribution (for increasing extent of reaction or for decreasing ϕ) perturbing a quantitative analysis, as evidenced in Figure 3. Already at $\phi_0 = \phi^*$, $I_{\text{stat}}(q)$ and $I_{\text{dyn}}(q)$ are of similar magnitude for $q \rightarrow 0$, whereas for larger ϕ_0 , the relevance of the static contribution fades out. This particular behavior is discussed in more detail in Section 5. Based upon this comparison, we

conclude that ξ_0 as determined from I_{dyn} provides the correct estimate of the solution-like correlation length inside the sample, as opposed to ξ_{all} determined from the entire scattering intensity, even though the full scattering signal at preparation conditions I_{all} in Figure 2 appears to be well approximated by I_{F} .

For the static correlation length Ξ related to the heterogeneous time average density, at preparation conditions, we find that all data are slightly curved as a function of ϕ_1 and that they do not follow a single scaling law. Therefore, we have not attempted to determine an apparent exponent α . Slices through the corresponding time average density profiles of the networks are shown in the bottom right part of Figures S2, S4, and S6 for the preparation conditions at ϕ^* , $2\phi^*$, and $4\phi^*$, respectively. For the lowest concentration, these density profiles follow essentially the positions of the star centers. For larger concentrations, the high density around the star centers becomes less visible as the average ϕ increases. We return to this point in Section 5 when discussing the physics behind the correlation length Ξ in more detail.

Finally, we have also analyzed the scaling relations based upon the effective ϕ_1 in aperiodic samples, which is required to correctly test scaling relations between the as-prepared state and swelling equilibrium, see ref 25 for more details. The role of ϕ_1 is to compensate for the impact of boundary effects on the effective size of the sample by virtually cutting off all parts in the periphery of the system falling significantly below the effective density in the middle. For computing the scattering data, we have avoided such cuts as sharp boundaries produce strong additional scattering signals (the following subsection provides an example for this effect). This discrepancy and the systematic shift of ϕ_1 with respect to ϕ_0 lead to slightly enhanced exponents α for the preparation state. We expect a similar enhancement for the swelling equilibrium that cancels out (similar to the analysis of the preceding work²⁵) when relating the polymer volume fraction ϕ at swelling equilibrium with the ϕ_0 in the preparation state.

4.2. Scattering Data at Swelling Equilibrium. In aperiodic networks prepared in a box size of $L = 512u$ and swollen to equilibrium in a larger box $L = 800u$, the presence of a fuzzy sample surface further complicates the data analysis. Now, the static part of the scattering intensity $I_{\text{stat}}(q)$ has to account both for the inhomogeneous density inside the sample and for a surface term arising from the shape of the finite network sample. As the shape of each swollen polymer sample corresponds to a somewhat irregular rounded cube, compare Figures S3, S5, and S7, an overall form factor cannot easily be parametrized, so that an approximation like a HS according to eq 16 comes to its limits. For simplicity, we approach the surface term by the Debye–Bueche function according to eq 18, and we consider it as a second contribution to the static scattering intensity

$$I_{\text{stat}}(q) = I_{\text{G}}(q) + I_{\text{DB}}(q) \quad (23)$$

Following the same strategy as in Section 4.1, we first fit $I_{\text{F}}(q)$ from eq 11 to the dynamic part of scattering, $I_{\text{dyn}}(q)$, again with an amplitude determined in the range $0.01/u \leq q \leq 0.05/u$ and a correlation length in the range $0.6/u \leq q \leq 1/u$, and in a second step, we assign $I_{\text{G}}(q) + I_{\text{DB}}(q) + I_{\text{F}}(q)/X$ with $X = 100$ to $I_{\text{stat}}(q)$. An example for the data at swelling equilibrium (sample prepared at $\phi_0 = 2\phi^*$) is given in Figure 5. Residual deviations arising from the star hump contributing to $I_{\text{dyn}}(q)$ occur in the region $0.1/u \leq q \leq 0.25/u$, but they are

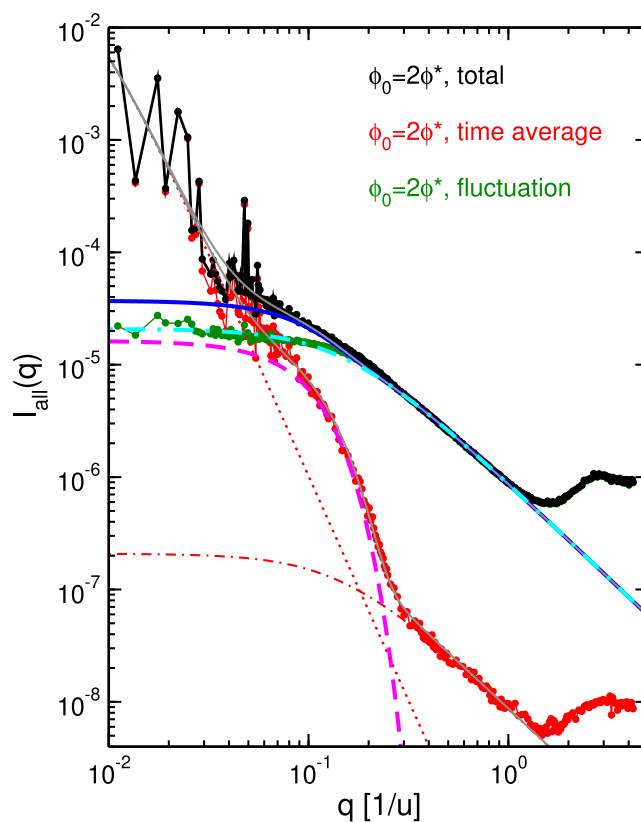


Figure 5. Scattering data from a network with $N = 43$, prepared at $\phi_0 = 2\phi^*$ in a box of $L = 512u$ and swollen to equilibrium in a larger box $L = 800u$. The total scattering intensity $I_{\text{all}}(q)$ (black dots) is split into the static part $I_{\text{stat}}(q)$ (red dots) and the dynamic part $I_{\text{dyn}}(q)$ (green dots). Lines visualize fit functions: fit of $I_{\text{dyn}}(q)$ for $q < 1/u$ excluding the region of the star hump with $I_{\text{F}}(q)$ (cyan dashed-dotted); fit of $I_{\text{stat}}(q)$ over the range $q < 1/u$ with $I_{\text{G}}(q) + I_{\text{DB}}(q) + I_{\text{F}}(q)/X$ (gray solid), $I_{\text{G}}(q)$ (magenta dashed), $I_{\text{DB}}(q)$ (red dotted), and $I_{\text{F}}(q)/X$ (red dashed-dotted). The blue curve shows the sum of model functions excluding the surface term, i.e., $I_{\text{G}}(q) + I_{\text{F}}(q)$. The curve superimposed to $I_{\text{all}}(q)$ (gray) shows the sum of the model functions, $I_{\text{G}}(q) + I_{\text{DB}}(q) + I_{\text{F}}(q)$. Averages are calculated over $X = 100$ frames.

significantly reduced with respect to the same sample at preparation. As expected, at large wave vectors, the static scattering intensity $I_{\text{stat}}(q)$ follows the same shape as $I_{\text{all}}(q)$ or $I_{\text{dyn}}(q)$, scaled down by a factor $1/X$. For a small q , the surface term $I_{\text{DB}}(q)$ dominates, but over an intermediate range $0.06/u < q < 0.25/u$, frozen density inhomogeneities with their Gaussian shape $I_{\text{G}}(q)$ exceed the surface term. Hence, the bulk part of the static intensity $I_{\text{stat}}(q)$ according to $I_{\text{G}}(q) + I_{\text{F}}(q)/X$ and the bulk part of the total intensity $I_{\text{all}}(q)$ following $I_{\text{G}}(q) + I_{\text{F}}(q)$ can clearly be discerned, revealing that toward $q \rightarrow 0$, contributions to $I_{\text{all}}(q)$ arising from static disorder parametrized as $I_{\text{G}}(q)$ are only slightly smaller than the dynamic part fitted with $I_{\text{F}}(q)$.

Figure 6 presents scattering data from samples swollen to equilibrium, over a broad range of polymer volume fractions at preparation. For all data, the same analysis was performed, allowing us to split the data into contributions $I_{\text{G}}(q)$, $I_{\text{DB}}(q)$, and $I_{\text{F}}(q)$. The model functions provide a good description of the simulation data. In particular, at small polymer volume fractions $\phi_0 \leq \phi^*$, around $q = 0.15/u$, the hump in the star factor results in clearly visible residual deviations between model functions and simulation data. On average, the ratio

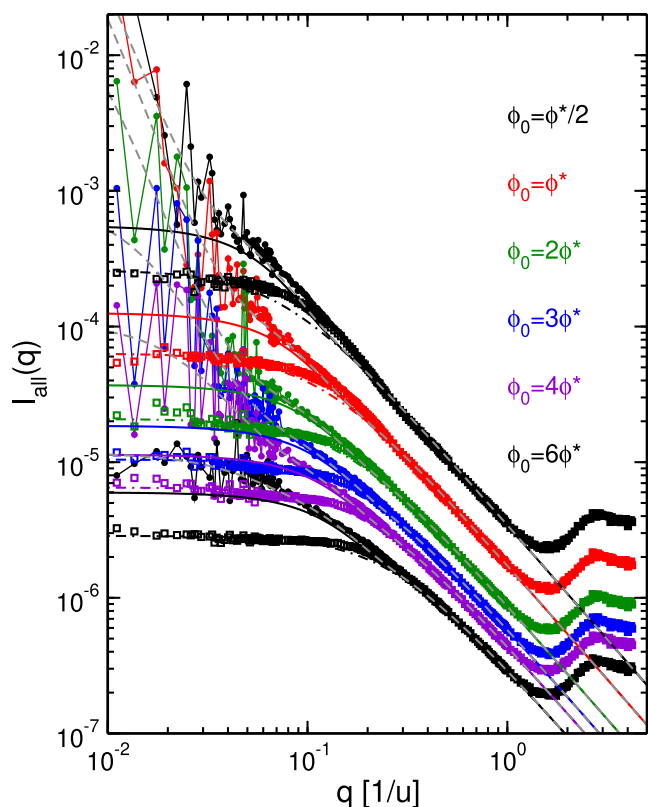


Figure 6. Scattering data from star networks prepared in a box $L = 512u$ and swollen to equilibrium in a box $L = 800u$, denoted according to the polymer volume fraction ϕ_0 at preparation: scattering intensity $I_{\text{all}}(q)$ (colored dots), dynamic part of scattering intensity $I_{\text{dyn}}(q)$ (colored open squares), total model curve $I_G(q) + I_{\text{DB}}(q) + I_F(q)$ (gray dashed), fit to $I_{\text{dyn}}(q)$ with $I_F(q)$ (colored dashed-dotted), and model curves without surface term $I_G(q) + I_F(q)$ (solid lines), where $I_G(q)$ was derived from fitting the static intensity $I_{\text{stat}}(q)$ with the model function $I_G(q) + I_{\text{DB}}(q) + I_F(q)/X$ as shown in Figure 5 for $\phi_0 = 2\phi^*$.

$I_G(q)/I_F(q)$ extrapolated toward $q \rightarrow 0$ is slightly below unity, with little variations from sample to sample (see the following sections for more details).

In Figure 7, we show representative fit results for the correlation lengths of the swollen networks after splitting the data into a dynamic and a static contribution. These data are compared with an analysis of $I_{\text{all}}(q)$ using a sum of eqs 11 and 18, with parameters of the surface term $I_{\text{DB}}(q)$ determined in a fit of the static part $I_{\text{stat}}(q)$. Power law fits of the correlation lengths as a function of polymer volume fraction might exclude the data at the largest or lowest volume fraction, respectively, if deviating from the trend of all other data, see Table S1 for further details. With this restriction, the data for ξ and ξ_{all} are well reproduced by a single power law. The results of all power law fits are summarized in Table 1. Similar to the preparation state, we observe that all estimates for ξ_{all} significantly exceed the results for ξ after splitting the data into a static and a dynamic contribution. Moreover, all exponents for fitting the ξ_{all} data exceed the corresponding estimates for ξ in Table 1, whereby the latter are clearly closer to the theoretical prediction for polymer solutions.

The correlation lengths ξ of the networks at swelling equilibrium and at preparation conditions fall on top of each other for networks with the same N , if these are analyzed at the same polymer volume fraction, see Figure 8. This coincidence

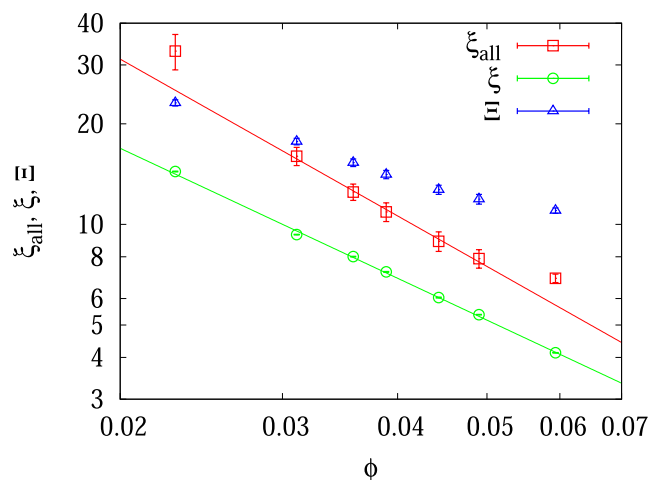


Figure 7. Correlation lengths in units of u , for $N = 43$. The correlation length ξ (green) is derived from the dynamic part of the scattering intensity $I_{\text{dyn}}(q)$; the correlation length ξ_{all} (red) is obtained from the total scattering intensity $I_{\text{all}}(q)$. The static correlation length Ξ derived from $I_{\text{stat}}(q)$ (blue) is included for completeness. The exponents obtained from power law fits $\propto \phi^{-\alpha}$ are summarized in Table 1.

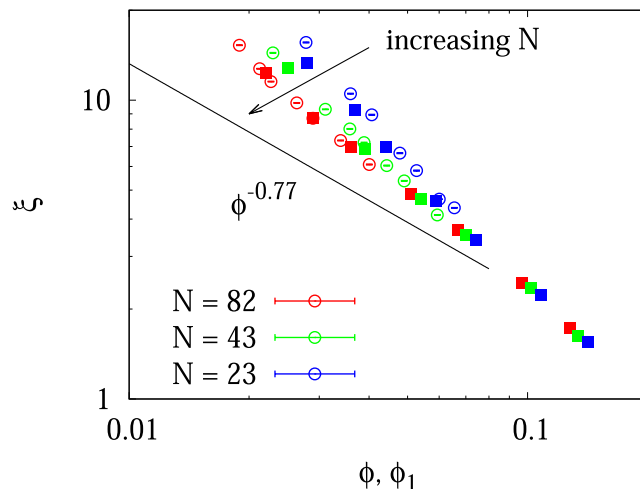


Figure 8. Comparison of the correlation length ξ at swelling equilibrium (open symbols) and under preparation conditions (closed symbols). The solid line visualizes the expected scaling relation $\xi_{\text{sol}} \propto \phi^{-\nu/(3\nu-1)} \propto \phi^{-\alpha}$ for a polymer in a good solvent, with $\alpha \approx 0.77$.

encodes the fact that ξ is a unique function of the polymer volume fraction, supporting the fact that our approach provides a reliable analysis of the scattering data. Differences between sets of data with different N are systematic and must result from the different cross-link concentration in the samples. A larger cross-link concentration leads to a larger contribution of the star hump for smaller N at the same ϕ . This enlarges the apparent ξ for smaller N . This is exactly what is observed in Figure 8 for low ϕ . As mentioned above, this effect plays no role for the largest ϕ as the star hump is then located at a too low q to interfere with a determination of ξ .

In comparison with ξ_{all} , we conclude that the correlation length ξ provides a correct analysis of the solution-like correlation length inside the network, however under the constraint that the impact of the star hump on the determination of ξ has to be minimized by the procedure applied in our data analysis. The fact that the entire scattering

intensity $I_{\text{all}}(q)$ can be interpolated smoothly with a single fractal model function based upon a correlation length ξ_{all} is not a sufficient indication for the absence of static contributions to the scattering intensity. Since Ξ is described by a different model function, see eq 20, this can lead to an interpretation of the scattering data through a single correlation length ξ_{all} , significantly exceeding even the true static correlation length Ξ at a low polymer volume fraction, see Figures 4 and 7. Hence, a quantitative discussion of the gels based upon ξ_{all} is likely to produce inconsistent results. Therefore, we omit a broader comparison with preceding experimental data based upon ξ_{all} , and we recommend to split the data into a “static” and a “dynamic” contribution, providing Ξ and ξ , respectively.

5. WHAT IS THE ORIGIN OF THE STATIC CORRELATION LENGTH?

The bottom right part of Figures S2–S7 of the Supporting Information shows the time average density of the networks carrying all the information about the static correlation length. According to these figures, the time average density mainly follows the positions of the star centers at low ϕ , whereas this effect becomes increasingly invisible for $\phi \rightarrow 1$ as the average polymer density increases. A larger polymer density around the star centers leading to a larger central blob was discussed some time ago for solutions of star polymers.¹⁰³ At swelling equilibrium, each correlation volume stores about kT of elastic energy for balancing the osmotic pressure. Thus, at swelling equilibrium, the larger blobs around the cross-links can be considered as being localized within their own diameter, such that Ξ provides an estimate of the size of these cross-link blobs (up to a numerical coefficient of order unity). The localization of the cross-link blobs can be modeled by a harmonic confining potential, often expressed in the form of ideal virtual chains, see, e.g., refs 104–106. The shape of the harmonic confining potential implies a Gaussian density distribution of the cross-link positions, leading in a first approximation to a Gaussian contribution to the scattering intensity arising from the cross-link blobs. This explains the good agreement of the Gaussian term with the simulated scattering data. The role of cross-link dynamics was first proposed in ref 101. According to the above reasoning, dynamics cannot be separated from the scaling of the size of the cross-link blob at swelling equilibrium as the blobs are held in space within a distance proportional to their own size. This condition is not satisfied under preparation conditions or during deswelling of the networks, allowing for a fundamental test of the above ideas.

The above idea of the denser cross-link blobs and the split of the scattering signal into a static and a dynamic component is illustrated in Figure 9. The landscape shows a slightly smoothed version of the time average density profile in a thin slice through the network shown in the sky. The glassy spheres on top sketch cross-link blobs moving around their time average positions indicated by the white anchors. Domain size and displacement have roughly the same size, and both establish the diameter of a typical mountain, as measured through the static correlation length Ξ . For the labeled anchor in the foreground, the displacement is quite large but still within the blob size shown by the shadow of the blob on the ground. The effective diameter of a mountain top is a combination of cross-link blob size and motion, where a partial superposition of adjacent blobs might play an additional role.

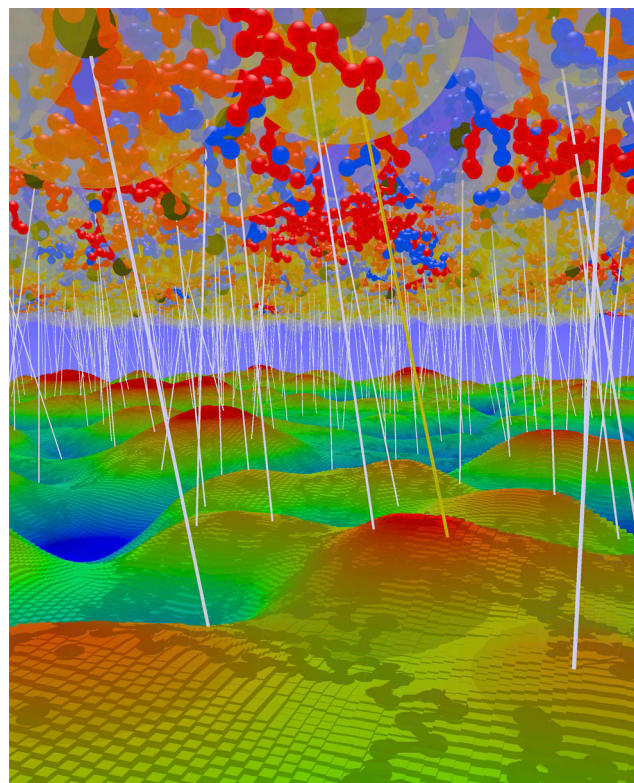


Figure 9. Time average density landscape (bottom) of a thin slice (20 lattice units thick) through a network (snapshot shown on top) including the denser cross-link blobs (glass spheres) around the cross-links (large black monomers). The top end of the white cylinders visualizes the random motion of the cross-links around their time average position (bottom end), establishing the mountains of the density landscape. Cross-links and blobs were selected for the plot according to the position in the snapshot and not according to the time average position (some may have moved in or out of the slice temporarily). For better visibility, one anchor in the foreground is shown in yellow, and the corresponding cross-link blob has a reduced transparency. The length unit of the density landscape refers to the length unit of the lattice. Monomer size is reduced by a factor of 2 to allow a better view into the structure; cross-links are enlarged to improve visibility. For visualization, the noise of the density landscape was damped out by averaging over neighboring points within a distance of 5 lattice units. The slice is taken from the network at $2\phi^*$ with $N = 43$ at equilibrium swelling.

A rough estimate for the size of a larger “cross-link blob” can be obtained by equating the local monomer volume fraction around the star center with the total volume fraction ϕ . For our simulation model, each monomer occupies 8 lattice units, $v_0 = 8u^3$. In the following, we use N_a to count the monomers along the star arms so that the first monomer next to the star center is $N_a = 1$. Then, we can estimate the polymer volume fraction around the star center as a function of N_a by considering a spherical volume with a radius reflecting the average star size up to monomer N_a

$$\phi(N_a) \approx \frac{3v_0(fN_a + 1)}{4\pi b^3 N_a^{3\nu}} = \phi \quad (24)$$

For simplification, we approximate $\pi \approx 3$ and $fN_a + 1 \approx fN_a$, giving a simplified scaling law for N_a

$$N_a \approx \left(\frac{v_0 f}{4\phi b^3} \right)^{1/(3\nu-1)} \quad (25)$$

The size of the cross-link blob (neglecting cross-link motion) is then estimated through the radius of gyration of a self-avoiding star with N_a segments per arm. In the limit of small $f = 4$, we keep the branching coefficient of ideal stars and adapt only the scaling of the star arms in a first approximation, as proposed in a preceding work.¹⁰⁷ This leads to

$$\Xi \approx b \frac{(3 - 2/f)^{1/2}}{\delta^{1/2}} N_a^\nu \approx b \frac{(3 - 2/f)^{1/2}}{\delta^{1/2}} \left(\frac{v_0 f}{4\phi b^3} \right)^{\nu/(3\nu-1)} \quad (26)$$

The dependence on polymer volume fraction is $\propto \phi^{-0.77}$ in the a-thermal limit ($\nu \approx 0.5876$) and crosses over to $\propto \phi^{-1}$ in the concentrated regime ($\nu = 1/2$) for theta solvents. For $f = 4$ and $b \approx 2.73u$ at low ϕ , we obtain $\Xi \approx 0.86u\phi^{-0.77}$ as a rough quantitative estimate. In the top part of Figure 10, a fit to the Ξ data of all swollen samples leads to $\Xi \approx (1.1 \pm 0.2)u\phi^{-0.80 \pm 0.03}$, in almost quantitative agreement with the expected scaling. To further corroborate our analysis, in Figure 10, we also include the root-mean-square distance of the cross-link motion in space, δR . All data on cross-link dynamics are perfectly aligned with Ξ , providing a strong argument that the static correlation length reveals the fluctuating position of the cross-link domains and that the cross-link motion remains confined to a volume comparable to the size of the cross-link blob. Remarkably, even the outliers in both sets of data, Ξ and δR , show the same trend. A quantitative comparison reveals $\Xi \lesssim \delta R$, whereas one might expect roughly $\Xi^2 \approx 2\delta R^2$, as both blob size and blob motion should contribute to the apparent Ξ . However, this simple expectation ignores a possible partial screening of the visible size and position of the cross-link blob by the surrounding blobs.

This latter point becomes more apparent at preparation conditions, where we expect that the contribution of the cross-link motion to Ξ becomes more prominent. To elucidate this point, in the bottom part of Figure 10, we compare our results for Ξ with the root mean square distance of the cross-link motion in space, δR_0 . We observe that for sufficiently large $\phi > \phi^*$, the cross-link motion runs parallel to the measured correlation length Ξ , where Ξ remains clearly below the cross-link motion. Therefore, we conclude that Ξ encodes a combination of the cross-link motion (as proposed in ref 101) enlarged by the cross-link blob size, whereas the apparent Ξ is screened in part by the surrounding correlation volumes of the network. This statement holds at least for the model networks of the present study, but it will require further tests for other network architectures.

This hypothesis can be corroborated by analyzing the scattering intensities in the limit of $q \rightarrow 0$, in particular, the ratio $I_G(0)/I_F(0)$. At swelling equilibrium and under preparation conditions of $\phi_0 \approx \phi^*$, for our network architecture, we expect that nearly all monomers are in the cross-link blobs, and thus, all of them contribute to I_G . Because all monomers have a share in the solution-like scattering accounting for the form factor in the semidilute solution, at swelling equilibrium and for preparation at $\phi \lesssim \phi^*$, we estimate that

$$I_G(0) \approx I_F(0) \quad (27)$$

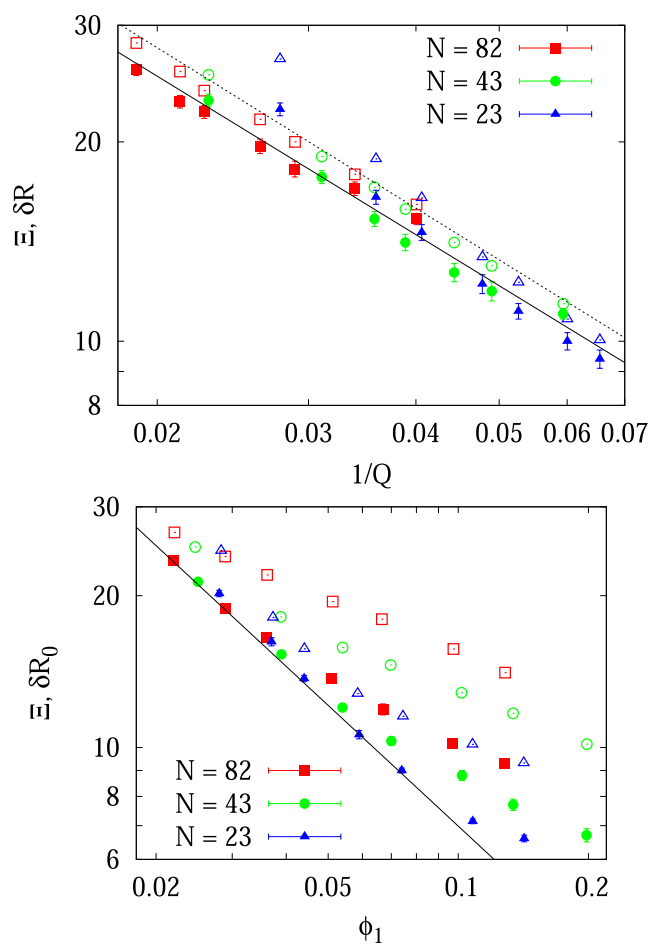


Figure 10. Top: static correlation length Ξ as a function of polymer volume fraction $\phi = 1/Q$ at swelling equilibrium (filled symbols) compared with the length δR describing the root-mean-square displacements of the cross-links (open symbols). The continuous line is a power law fit to all Ξ data at swelling equilibrium $\propto (1/Q)^{-0.80 \pm 0.03}$, the dashed line is a similar fit to the δR data $\propto (1/Q)^{-0.80 \pm 0.05}$. Bottom: same analysis as in the top part under preparation conditions, using the same colors and symbols as above for the same sets of networks. The continuous line is the fit to the data at swelling equilibrium taken from the top part. Data for δR and δR_0 were taken from Table 1 of ref 25.

For preparation states with $\phi_0 > \phi^*$, we assume that the cross-link blobs are dilute and cover only a portion of all monomers, decreasing as $N_a \propto \phi_0^{-1/(3\nu-1)}$ for increasing ϕ_0 . If these denser blobs are smeared out over a larger volume by the motion of the blob, the correlation length will increase accordingly, but the time average excess density (as compared to the time average density of the solution) will be reduced inversely to the volume change, keeping the excess polymer content time invariant. Recall that the scattering intensity in dilute solutions (for the dilute cross-link blobs) is proportional to the molar mass of the scattering objects and to their concentration. Therefore, the ratio of the scattering intensities $I_G(0)$ and $I_F(0)$ is expected to decay as

$$\frac{I_G(0)}{I_F(0)} \approx \left(\frac{\phi^*}{\phi_0} \right)^{1/(3\nu-1)} \quad (28)$$

reflecting the concentration-dependent change of the excess polymer per cross-link blob for all samples prepared at $\phi_0 >$

ϕ^* . This dependence agrees with other theoretical predictions, see, e.g., eq 5.43 of ref 108.

Both predictions for swelling equilibrium and preparation state are tested in Figure 11. The exponent describing the

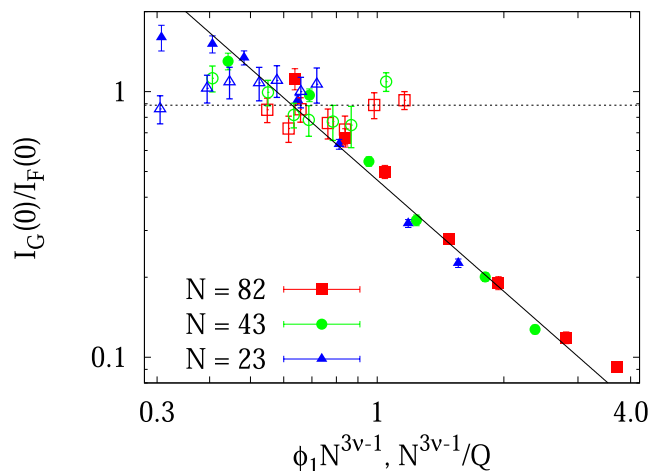


Figure 11. Intensity ratio $I_G(0)/I_F(0)$ related to the respective correlation lengths Ξ and ξ under preparation conditions (filled symbols) and at swelling equilibrium (open symbols). The continuous line $\propto \phi_1^{-1.39 \pm 0.05}$ is a fit to the data with $\phi_1 N^{3v-1} > 0.5$ under preparation conditions. The dashed line is a fit with a constant $c = 0.89 \pm 0.03$ to all data at swelling equilibrium.

scaling of the intensity ratio at preparation conditions is close to the exponent of -1.31 for $\nu = 0.5876$ predicted in eq 28. This is another indication that the cross-link blobs are the origin of the excess scattering at preparation conditions. Moreover, the data at swelling equilibrium are well described by a constant slightly below unity. Here, ref 108 predicts in eq 5.44 that $I_G(0)/I_F(0) \approx (\phi_0/\phi^*)^{5/16} \gg 1$, which is not supported by our data. With respect to polymer gels of a different network architecture, our analysis benefits from the nearly constant amount of network defects, see Figure 2 of ref 25. Increasing weight fractions of network defects will reduce the above ratios because defects are less localized than network junctions and do not contribute to $I_G(0)$ in a first approximation. If the volume fraction of the defects develops a significant dependence on ϕ_0 , this will result in further corrections of the observed ratio of $I_G(0)/I_F(0)$ on top of additional corrections for swelling equilibrium.¹⁰⁹ Altogether, the static scattering data of model networks at swelling equilibrium could also provide a quantitative estimate for the amount of network defects. This hypothesis will be tested in future work.

Experimental data for end-linked model networks or model networks based upon a heterocomplementary coupling of star polymers are not abundant, in particular, when seeking for scattering data analyzed by a combination of a Gaussian and an Ornstein–Zernike function or its equivalent for fractal dimension as in our analysis. Moreover, in order to test the scaling relations proposed above, a sufficiently broad regime of ϕ and ϕ_0 needs to be covered. We found only two works in the literature^{101,110} satisfying most of these conditions. In ref 110, an average concentration dependence of $\Xi \propto \phi^{-0.63}$ was reported for equilibrium swelling, in good agreement with the general trend of our data, see Figure 10. The scattering intensities scale as $I_G(0) \propto \phi^{-1.45}$ and $I_F(0) \propto \phi^{-0.51}$,¹¹⁰

providing a scaling of the ratio $I_G(0)/I_F(0) \propto \phi^{-0.92}$, clearly weaker than in our samples. The data in ref 110 were obtained from end-linked model networks, where pending loops are not suppressed by the network architecture. This decreases the growth of the static contribution toward smaller ϕ , leading to a weaker concentration dependence than expected. Figure 3 of ref 101 reports a much weaker apparent concentration dependence of $\Xi \propto \phi^{-0.12 \pm 0.06}$ for end-linked model networks. Here, three samples reached rather similar equilibrium degrees of swelling and a nearly constant intensity ratio varying between 0.41 and 0.52. We take the lower intensity ratio at swelling equilibrium as an indication of a larger defect fraction in the experiments as compared to our model systems. The rest of the data in Figure 3 of ref 101 refer to the deswelling of the third sample. The authors of ref 101 expected a concentration dependence of $\Xi \propto \phi^{-1/3}$ for this process by assuming that the correlation length shrinks with the sample size upon deswelling, and they correlated the weaker dependence with the swelling of chain size in solution. This discussion, however, is partially misleading, as the average chain size is expected to shrink $\propto \phi^{-1/3}$ upon deswelling.¹¹¹ During swelling, the cross-link motion changes in good approximation like the reference size⁹⁷ of the polymer chains in the corresponding polymer solution $\propto \phi^{-(\nu-1/2)/(3\nu-1)} \propto \phi^{-0.11}$, see also Figure 3 of ref 25. Thus, the observed scaling during deswelling is another indication that the cross-link dynamics dominate the apparent size of Ξ for volume fractions above the swelling equilibrium. Altogether, preceding observations are in accord with our data, our discussion, and the model proposed above.

6. DISCUSSION

We have analyzed a large set of scattering data from computer simulations of star networks by decomposing the scattering intensity into a time average “static” part and a “dynamic” component. This decomposition is mandatory to extract a reliable estimate for the liquid-like correlation length ξ . This correlation length can carry information about the star hump in an appropriate range of concentrations around the overlap polymer volume fraction of the solution of star polymers, ϕ^* .⁹³ This leads to a stronger apparent concentration dependence of the correlation length when analyzed in the standard way based upon the Ornstein–Zernike function or its fractal generalization. As compared to end-linked model systems, the star polymer solution already carries the star hump correction, leading to a low excess scattering of a star polymer network compared to the corresponding star solution. This observation is supported by experimental data,^{31,93} but in preceding works, it has been interpreted in a different manner. For increasing concentrations clearly above the overlap concentration, the star hump becomes suppressed by a decreasing ξ so that it becomes nearly invisible, as also supported by experimental scattering data.^{31,33} However, this observation is not necessarily an indication of a more homogeneous network structure, because the comparison with the precursor solution relies on different reference systems when investigating different network architectures, like, e.g., end-linked model networks or networks made by a cross-linking copolymerization process of stars. If the molecular structure of the reference system is closer to the final network structure, certainly, a better agreement between both can be expected.

In the literature, the emergence of a static correlation length has been associated with a large number of different structural units or processes. For instance, Ξ was associated with the size

of a network coil in refs 79 and 112 based upon a set of model equations differing from ours. If such an idea is correct, a scaling of the static correlation length proportional to the coil size $\propto \phi^{-(\nu-1/2)/(3\nu-1)} \approx \phi^{-0.11}$ can be anticipated. We observe such a scaling for the real space data of the network chains, however, the scaling of the data in Figures 4 and 7 does not follow this trend.

In other work, cyclic structures in the networks^{58,113,114} were suspected to cause the static correlation length. Similar to network coils, the obvious argument is that the static correlation length must be related in some form to network elasticity because the static contribution is absent for the solutions. Network elasticity emerges through the network cycles.¹¹⁵ However, the scaling of the size of characteristic cycles in the network, i.e., the peak of the shortest cycles, varies only a little for $\phi_0 > \phi^*$, see, e.g., Figure 3 of ref 116. We have checked this point explicitly, even though it can be anticipated from the slow change in the network connectivity as a function of ϕ , see Figure 2 of ref 25. Altogether, the scaling of the size of the characteristic loops is not much different from the scaling of chain size and does not fit to the scaling of Ξ under preparation conditions.

Another idea to explain the emergence of a static correlation length Ξ is the formation of more densely linked regions in the network^{117,118} (qualitatively similar is the discussion in ref 108 when approaching the cross-link saturation threshold). Our networks are not close to the cross-link saturation threshold, and there are no larger densely linked regions in space, except for some domains with nonreactive groups (see below for more details). Therefore, our simulation data provide no conclusions in this direction. However, there are works in the literature allowing us to sharpen the conditions for the “more densely linked regions”. Random fluctuations in the cross-link concentration far from the cross-link saturation threshold seem to remain insufficient for a qualitatively different picture: the simulations of ref 58 and experimental data¹¹⁹ show no significant difference between the scattering data of end-linked and randomly cross-linked model networks if these have a comparable degree of swelling, a comparable weight fraction of network defects, and a comparable average degree of polymerization of the network strands. This observation is also supported by theoretical work showing that the molar mass distribution of network strands does not affect the phantom modulus.¹²⁰ One systematic difference is that the cross-links in the randomly linked sample develop a somewhat stronger localization,^{17,120} i.e., a smaller Ξ , roughly compensating for the increase of the apparent weight-average molar mass per cross-link because of polydisperse arms.¹²¹ Therefore, a more heterogeneous network than expected from a comparison with near ideal end-linked model networks^{58,119} or irradiation cross-linked samples¹²² is more likely an indication of mixing issues related to the dispersion of the cross-links if the cross-link density does not approach the cross-link saturation threshold.

Mixing problems always occur when more than one component establishes the network structure. For our perfectly mixed and stoichiometrically balanced systems, the statistical positioning of A and B stars creates a local stoichiometric imbalance freezing during the cross-linking process. Then, spatial domains of nonreacted arm ends of one particular type of star can form. This scenario is visualized with our simulation data in the bottom left of Figures S2–S7 in the Supporting Information. Here, the time average positions of the non-

reacted groups in a thin slice of the network are superimposed to a density map, showing which of the two types of stars dominates the polymer density in a particular region in space. The overlay demonstrates that larger spatial regions with a dominance of either type of polymer can cause the formation of domains accumulating nonreacted groups. The underlying composition fluctuations are known to dominate the long time reaction kinetics¹²³ for a stoichiometrically balanced system, producing similar domains and patterns for end-linked model networks, see Figure 1 of ref 124. Poor mixing, on the other hand, may even cause a shift of the expected gel point or a stronger slowdown of reaction kinetics toward high conversion,¹²⁵ which could be tracked by analyzing reaction kinetics. Remarkably, computer simulations⁵⁵ and more recent experiments on stoichiometrically mixed end-linked model networks^{44,126} reach conversions p in the range of 98–99%. For these systems, we expect only a minute effect of the few missing bonds in the system. For the particular case of our model systems with $p = 0.95$, we find an increasing number of 2–4 domains in one direction across the sample with increasing ϕ , compare Figures S2–S7. In any case, this would be related to a Ξ of about 100 lattice units or larger. Our results for Ξ do not reach such length scales. Moreover, the accessible q range is not large enough to completely exclude the relevance of these domains. Thus, we can only comment that statistical mixing could become a possible correction that will set in on length scales clearly beyond Ξ for our network architecture. It remains an open problem for future research to understand the excess scattering resulting from a controlled degree of imperfection in mixing the network components. If that can be achieved, scattering data at low q could be used as a quantitative tool for quality control.

It has been proposed that network defects or topological inhomogeneities might contribute to excess scattering.^{36,127} Network defects in the classical sense are characterized by the property that they are attached to the network only through one single point.¹¹⁵ Such defects do not contribute to elasticity because they can freely reorient inside the network. If the network structure is heterogeneous, producing local polymer density gradients, defects will orient (on a time average basis) down the gradient, similar to the orientation of the chains in a polymer brush.^{128,129} This latter effect was observed in a simulation study where networks with a controlled heterogeneity were prepared and swollen to equilibrium:¹²⁵ in the preparation state, the concentration of the elastically active material of sample C1 of this study formed a big hole, reaching zero concentration in the middle. At swelling equilibrium, the polymer content in the hole was not zero, but instead, it remained above 50% of the peak polymer content because of network defects that were oriented toward the hole. In total, because of network defects, the local density fluctuations of the network were smaller than the density fluctuations of the elastic network. This partially contradicts the role attributed to network defects in the literature, see, e.g., Section 2 of ref 36. The problematic point in preceding discussions is that often a regular network is taken as a reference, where single chains are cut randomly to create defects. Such a situation is never realized in real networks, and the degree of randomness of the network will hardly change upon cutting or connecting single bonds. Nevertheless, we have checked our star networks for pending arms or other less ideal local structures. These are shown in the top right part of Figures S2–S7, but we could not identify a correlation between their location and an increase of

the time average concentration beyond what can be expected from the network architecture and connectivity (e.g., pending arms are still tied to the junction, and they contribute roughly the same way to the cross-link blobs as nonpending arms). In fact, the common point of these less ideal structures is that the corresponding chains are less localized inside the network. Therefore, these structures are more susceptible for equilibrating local time average concentration gradients. This, in effect, reduces existing time average density gradients instead of creating them.

7. CONCLUSIONS

Our analysis supports the fact that the static correlation length Ξ is related to a superposition of the root-mean-square distance a cross-link can move, δR , and the size of the denser cross-link blob $\propto \xi$. At swelling equilibrium, the root-mean-square displacement of the cross-links locks in at a length $\propto \xi$, leading to $\Xi \propto \xi$ at swelling equilibrium. For the nearly perfect networks in the nonentangled limit of our study, the scattering intensities at swelling equilibrium related to the dynamic contribution, $I_F(q)$, and to the static contribution, $I_G(q)$, are nearly identical in the limit of $q \rightarrow 0$. Thus, the network essentially only consists of cross-link blobs at swelling equilibrium. While this observation is well supported by our simulation data for the nonentangled limit, it must not extend toward the entangled limit or to networks containing a large volume fraction of defects. At preparation conditions, it becomes evident that both δR and the cross-link blob size contribute to Ξ because the scaling of Ξ crosses over from a dependence close to $\propto \xi$ (for preparation volume fractions ϕ_0 close to the swelling equilibrium) toward a dependence following mainly δR (in the limit of large ϕ_0). The ratio of the scattering intensities I_G/I_F for $q \rightarrow 0$ decays by a power law following the polymer fraction that can be associated with the cross-link blobs. On a quantitative basis, the apparent Ξ is always lower than δR (under preparation conditions) or comparable to δR (at swelling equilibrium). Because the size of the cross-link blob must be contained in Ξ , this indicates that a part of the true domain size is screened by the surrounding correlation volumes. Qualitatively, the experimental data available in literature^{101,110} are in good agreement with our observations, as detailed in the preceding sections. Our results agree in part with the scenario proposed for the limiting case of low cross-link density (“far away from the cross-link saturation threshold”) in ref 108. One interesting difference is the intensity ratio at swelling equilibrium, whereas the expectation of a pronounced maximum or a shoulder in the fluctuating intensity at intermediate wave vectors q turns out to correspond to Benoit’s star hump, reducing to a small shoulder in the scattering intensity for small f .

Our work provides a new perspective for analyzing scattering data of polymer networks at least for computer simulations. We also expect that our results will find application for analyzing experimental data, as our work identifies a Gaussian decay as the correct model function to extract the contribution of the cross-link blobs. For the current work, we have focused on heterocomplementary coupled model networks made of star polymers to understand the generic contributions that must be present in any kind of polymeric network and gel. In future work, we intend to apply this knowledge along two different routes of investigations. First, we want to explore additional possibilities to label parts of a network^{56,57} to deepen our understanding of what structural information can

be extracted by scattering experiments. Second, we will step by step relax the model character of the networks toward more complex systems based upon vulcanization, cross-linking copolymerization, etc., for understanding known or expected differences between these classes of networks.^{130,131} It is our hope that we can decode characteristic features of these network classes for an improved analysis of the network structure.

■ ASSOCIATED CONTENT

SI Supporting Information

The Supporting Information is available free of charge at <https://pubs.acs.org/doi/10.1021/acs.macromol.3c02607>.

Fit results for ξ and Ξ ; data averaging; and thin slices through several networks under preparation conditions and at swelling equilibrium (PDF)

■ AUTHOR INFORMATION

Corresponding Author

M. Lang – *Institut Theorie der Polymere, Leibniz-Institut für Polymerforschung Dresden, Dresden 01069, Germany*;
orcid.org/0000-0003-3851-6670; Email: lang@ipfdd.de

Author

R. Scholz – *Institut Theorie der Polymere, Leibniz-Institut für Polymerforschung Dresden, Dresden 01069, Germany*

Complete contact information is available at:

<https://pubs.acs.org/doi/10.1021/acs.macromol.3c02607>

Author Contributions

†R.S. and M.L. contributed equally to the manuscript.

Notes

The authors declare no competing financial interest.

■ ACKNOWLEDGMENTS

This work has received funding from DFG via project FOR2811 under grant 397384169. Computational resources provided by the Center for Information Services and High Performance Computing (ZIH) of TU Dresden are gratefully acknowledged. Moreover, we thank our friends at the research network FOR2811 for stimulating discussions regarding our simulation data and analysis.

■ ADDITIONAL NOTE

^a2-d sheets and random walks have a fractal dimension $D_f = 2$, resulting in the same decay of the form factor $\propto q^{-D_f}$ on length scales between sheet thickness and sheet extension or random walk step size and length.

■ REFERENCES

- (1) Sievers, J.; Mahajan, V.; Welzel, P.; Werner, C.; Taubenberger, A. Precision Hydrogels for the Study of Cancer Cell Mechanobiology. *Adv. Healthcare Mater.* **2023**, *12*, 2202514.
- (2) Carpa, R.; Remizovschi, A.; Culda, C. A.; Butiuc-Keul, A. L. Inherent and Composite Hydrogels as Promising Materials to Limit Antimicrobial Resistance. *Gels* **2022**, *8*, 70.
- (3) Ying, B.; Liu, X. Skin-like hydrogel devices for wearable sensing, soft robotics and beyond. *iScience* **2021**, *24*, 103174.
- (4) Peppas, N. A.; Keys, K. B.; Torres-Lugo, M.; Lowman, A. M. Poly(ethylene glycol)-containing hydrogels in drug delivery. *J. Controlled Release* **1999**, *62*, 81–87.

- (5) Nicolson, P. C.; Vogt, J. Soft contact lens polymers: an evolution. *Biomaterials* **2001**, *22*, 3273–3283.
- (6) Marangoni, A. G. Organogels: An Alternative Edible Oil-Structuring Method. *Biomaterials* **2012**, *89*, 749–780.
- (7) Zohuriaan-Mehr, M. J.; Kabiri, K. Superabsorbent polymer materials: A review. *Iranian Polymer J.* **2008**, *17*, 451–477.
- (8) Ahmed, E. M. Hydrogel: Preparation, characterization, and applications: A review. *J. Adv. Res.* **2015**, *6*, 105–121.
- (9) Gottlieb, M.; Macosko, C. W.; Benjamin, G. S.; Meyers, K. O.; Merrill, E. W. Equilibrium Modulus of Model Poly(dimethylsiloxane) Networks. *Macromolecules* **1981**, *14*, 1039–1046.
- (10) Patel, S. K.; Malone, S.; Cohen, C.; Gillmor, J. R.; Colby, R. H. Elastic Modulus and Equilibrium Swelling of Poly(dimethylsiloxane) Networks. *Macromolecules* **1992**, *25*, 5241–5251.
- (11) Hild, G. Model networks based on ‘endlinking’ processes: synthesis, structure and properties. *Prog. Polym. Sci.* **1998**, *23*, 1019–1149.
- (12) Michalke, W.; Lang, M.; Kreitmeier, S.; Göritz, D. Comparison of topological properties between end-linked and statistically cross-linked polymer networks. *J. Chem. Phys.* **2002**, *117*, 6300–6307.
- (13) Lang, M.; Müller, T. Analysis of the Gel Point of Polymer Model Networks by Computer Simulations. *Macromolecules* **2020**, *53*, 498–512.
- (14) Zhong, M.; Wang, R.; Kawamoto, K.; Olsen, B. D.; Johnson, J. A. Quantifying the impact of molecular defects on polymer network elasticity. *Science* **2016**, *353*, 1264–1268.
- (15) Lang, M. Elasticity of Phantom Model Networks with Cyclic Defects. *ACS Macro Lett.* **2018**, *7*, 536–539.
- (16) Lin, T.-S.; Wang, R.; Johnson, J. A.; Olsen, B. D. Revisiting the Elasticity Theory for Real Gaussian Phantom Networks. *Macromolecules* **2019**, *52*, 1685–1694.
- (17) Lang, M. On the Elasticity of Polymer Model Networks Containing Finite Loops. *Macromolecules* **2019**, *52*, 6266–6273.
- (18) Gusev, A. A.; Schwarz, F. Molecular Dynamics Study on the Validity of Miller-Macosko Theory for Entanglement and Crosslink Contributions to the Elastic Modulus of End-Linked Polymer Networks. *Macromolecules* **2022**, *55*, 8372–8383.
- (19) Sakai, T.; Matsunaga, T.; Yamamoto, Y.; Ito, C.; Yoshida, R.; Suzuki, S.; Sasaki, N.; Shibayama, M.; Chung, U.-I. Design and Fabrication of a High-Strength Hydrogel with Ideally Homogeneous Network Structure from Tetrahedron-like Macromonomers. *Macromolecules* **2008**, *41*, 5379–5384.
- (20) Shibayama, M.; Li, X.; Sakai, T. Precision polymer network science with tetra-PEG gels – a decade history and future. *Colloid Polym. Sci.* **2019**, *297*, 1–12.
- (21) Schwenke, K.; Lang, M.; Sommer, J.-U. On the Structure of Star-Polymer Networks. *Macromolecules* **2011**, *44*, 9464–9472.
- (22) Lang, M.; Schwenke, K.; Sommer, J.-U. Short Cyclic Structures in Polymer Model Networks: A Test of Mean Field Approximation by Monte Carlo Simulations. *Macromolecules* **2012**, *45*, 4886–4895.
- (23) Nakagawa, S.; Yoshie, N. Star polymer networks: a toolbox for cross-linked polymers with controlled structure. *Polym. Chem.* **2022**, *13*, 2074–2107.
- (24) Rose, K. A.; Marino, E.; O’Byrne, C. S.; Murray, C. B.; Lee, D.; Composto, R. J. Nanoparticle dynamics in hydrogel networks with controlled defects. *Soft Matter* **2022**, *18*, 9045–9056.
- (25) Lang, M.; Scholz, R.; Löser, L.; Bunk, C.; Fribicz, N.; Seiffert, S.; Böhme, F.; Saalwächter, K. Swelling and residual bond orientations of polymer model gels: the entanglement-free limit. *Macromolecules* **2022**, *55*, 5997–6014.
- (26) Katashima, T.; Kudo, R.; Naito, M.; Nagatoishi, S.; Miyata, K.; Chung, U.-I.; Tsumoto, K.; Sakai, T. Experimental Comparison of Bond Lifetime and Viscoelastic Relaxation in Transient Networks with Well Controlled Structures. *ACS Macro Lett.* **2022**, *11*, 753–759.
- (27) Barney, C. W.; Sacligil, I.; Tew, G. N.; Crosby, A. J. Linking cavitation and fracture to molecular scale structural damage of model networks. *Soft Matter* **2022**, *18*, 4220–4226.
- (28) Mendes, E.; Lindner, P.; Buzier, M.; Boué, F.; Bastide, J. Experimental Evidence for Inhomogeneous Swelling and Deformation in Statistical Gels. *Phys. Rev. Lett.* **1991**, *66*, 1595–1598.
- (29) Mendes, E.; Girard, B.; Picot, C.; Buzier, M.; Boue, F.; Bastide, J. Small-angle neutron scattering study of end-linked gels. *Macromolecules* **1993**, *26*, 6873–6877.
- (30) Bastide, J.; Candau, S. Structure of Gels as Investigated by Means of Static Scattering Techniques. *The Physical Properties of Polymeric Gels*; Wiley, 1996; pp 143–210, Chapter 5.
- (31) Horkay, F.; Nishi, K.; Shibayama, M. Decisive test of the ideal behavior of tetra-PEG gels. *J. Chem. Phys.* **2017**, *146*, 164905.
- (32) Kawamura, T.; Urayama, K.; Kohjiya, S. Small angle X-ray scattering study on role of trapped entanglements in structure of swollen end-linked poly(dimethylsiloxane) networks. *J. Chem. Phys.* **2000**, *112*, 9105–9111.
- (33) Li, X.; Nakagawa, S.; Tsuji, Y.; Watanabe, N.; Shibayama, M. Polymer gel with a flexible and highly ordered three-dimensional network synthesized via bond percolation. *Sci. Adv.* **2019**, *5*, No. eaax8647.
- (34) de Gennes, P. G. *Scaling Concepts in Polymer Physics*; Cornell University Press: Ithaca, 1979.
- (35) Shibayama, M. Spatial inhomogeneity and dynamic fluctuations of polymer gels. *Macromol. Chem. Phys.* **1998**, *199*, 1–30.
- (36) Seiffert, S. Scattering perspectives on nanostructural inhomogeneity in polymer network gels. *Prog. Polym. Sci.* **2017**, *66*, 1–21. Topical Volume on Polymer Physics
- (37) Morozova, S.; Hitimana, E.; Dhakal, S.; Wilcox, K. G.; Estrin, D. Scattering methods for determining structure and dynamics of polymer gels. *J. Appl. Phys.* **2021**, *129*, 071101.
- (38) Benoit, H.; Decker, D.; Duplessix, R.; Picot, C.; Rempp, P.; Cotton, J. P.; Farnoux, B.; Jannink, G.; Ober, R. Characterization of Polystyrene Networks by Small-Angle Neutron Scattering. *J. Polym. Sci. B* **1976**, *14*, 2119–2128.
- (39) Hinkley, J. A.; Han, C. C.; Mozer, B.; Yu, H. Chain Deformations in Rubber. *Macromolecules* **1978**, *11*, 836–838.
- (40) Beltzung, M.; Picot, C.; Rempp, P.; Herz, J. Investigation of the conformation of elastic chains in poly(dimethylsiloxane) networks by small-angle neutron scattering. *Macromolecules* **1982**, *15*, 1594–1600.
- (41) Beltzung, M.; Picot, C.; Herz, J. Investigation of the Chain Conformation in Uniaxially Stretched Poly(dimethylsiloxane) Networks by Small-Angle Neutron Scattering. *Macromolecules* **1984**, *17*, 663–669.
- (42) Bastide, J.; Duplessix, R.; Picot, C.; Candau, S. Small-Angle Neutron Scattering and Light Spectroscopy Investigation of Polystyrene Gels under Osmotic Deswelling. *Macromolecules* **1984**, *17*, 83–93.
- (43) Sukumaran, S. K.; Beaucage, G.; Mark, J. E.; Viers, B. Neutron scattering from equilibrium-swollen networks. *Eur. Phys. J. E* **2005**, *18*, 29–36.
- (44) Beech, H. K.; Johnson, J. A.; Olsen, B. D. Conformation of Network Strands in Polymer Gels. *ACS Macro Lett.* **2023**, *12*, 325–330.
- (45) Bastide, J.; Herz, J.; Boué, F. Loss of affinity in gels and melts. *J. Phys. (Paris)* **1985**, *46*, 1967–1979.
- (46) Fernandez, A. M.; Sperling, L. H.; Wignall, G. D. Conformation of Polybutadiene in the Network State by Small-Angle Neutron Scattering. *Macromolecules* **1986**, *19*, 2572–2575.
- (47) Davidson, N. S.; Richards, R.-W. Dimensions of Labeled Chains in Randomly Cross-Linked Polystyrene Networks at Swelling Equilibrium by Small-Angle Neutron Scattering. *Macromolecules* **1986**, *19*, 2576–2588.
- (48) Tsay, H.-M.; Ullman, R. Small-Angle Neutron Scattering of Cross-Linked Polystyrene Networks. *Macromolecules* **1988**, *21*, 2963–2972.
- (49) Pyckhout-Hintzen, W.; Springer, T.; Forster, F.; Gronski, W.; Frischkorn, C. Small-Angle Neutron-Scattering Investigation of a Multilinked Polybutadiene Network Cross-Linked in Solution. *Macromolecules* **1991**, *24*, 1269–1274.

- (50) Kloczkowski, A.; Mark, J.; Erman, B. Correlations among Chains along a Cross-Linked Path in a Phantom Network and Their Characterization by SANS. *Macromolecules* **1992**, *25*, 2455–2458.
- (51) Straube, E.; Urban, V.; Pyckhout-Hintzen, W.; Richter, D. SANS Investigations of Topological Constraints and Microscopic Deformations in Rubberelastic Networks. *Macromolecules* **1994**, *27*, 7681–7688.
- (52) Straube, E.; Urban, V.; Pyckhout-Hintzen, W.; Richter, D.; Glinka, C. J. Small-Angle Neutron Scattering Investigation of Topological Constraints and Tube Deformation in Networks. *Phys. Rev. Lett.* **1995**, *74*, 4464–4467.
- (53) Ohira, M.; Tsuji, Y.; Watanabe, N.; Morishima, K.; Gilbert, E. P.; Li, X.; Shibayama, M. Quantitative Structure Analysis of a Near-Ideal Polymer Network with Deuterium Label by Small-Angle Neutron Scattering. *Macromolecules* **2020**, *53*, 4047–4054.
- (54) Lang, M.; Scholz, R. On the swelling of polymer network strands. *Macromol. Rapid Commun.* **2024**, 2400025.
- (55) Lang, M.; Müller, T. On the Reference Size of Chains in a Network and the Shear Modulus of Unentangled Networks Made of Real Chains. *Macromolecules* **2022**, *55*, 8950–8959.
- (56) Scholz, R.; Lang, M. **2024** in preparation.
- (57) Scholz, R.; Löser, L.; Saalwächter, K.; Lang in preparation.
- (58) Lang, M.; Sommer, J.-U. On the origin of the scattering of gels and swollen polymer networks. *Constitutive Models for Rubber V*, 2007; pp 147–156.
- (59) Asai, M.; Katashima, T.; Chung, U.-I.; Sakai, T.; Shibayama, M. Correlation between Local and Global Inhomogeneities of Chemical Gels. *Macromolecules* **2013**, *46*, 9772–9781.
- (60) Pütz, M.; Kremer, K.; Everaers, R. Self-Similar Chain Conformations in Polymer Gels. *Phys. Rev. Lett.* **2000**, *84*, 298–301.
- (61) Duering, E. R.; Kremer, K.; Grest, G. Structure and relaxation of end-linked polymer networks. *J. Chem. Phys.* **1994**, *101*, 8169–8192.
- (62) Kenkare, N. R.; Smith, S. W.; Hall, C. K.; Khan, S. A. Discontinuous Molecular Dynamics Studies of End-Linked Polymer Networks. *Macromolecules* **1998**, *31*, 5861–5879.
- (63) Müller, M.; Binder, K.; Schäfer, L. Intra- and Interchain Correlations in Semidilute Polymer Solutions: Monte Carlo Simulations and Renormalization Group Results. *Macromolecules* **2000**, *33*, 4568–4580.
- (64) Lee, N.-K.; Abrams, C. F.; Johner, A.; Obukhov, S. Arrested Swelling of Highly Entangled Polymer Globules. *Phys. Rev. Lett.* **2003**, *90*, 225504.
- (65) Lee, N.-K.; Abrams, C. F.; Johner, A.; Obukhov, S. Swelling Dynamics of Collapsed Polymers. *Macromolecules* **2004**, *37*, 651–661.
- (66) Carmesin, I.; Kremer, K. The bond fluctuation method: a new effective algorithm for the dynamics of polymers in all spatial dimensions. *Macromolecules* **1988**, *21*, 2819–2823.
- (67) Deutsch, H. P.; Binder, K. Interdiffusion and self-diffusion in polymer mixtures: A Monte Carlo study. *J. Chem. Phys.* **1991**, *94*, 2294–2304.
- (68) Müller, T.; Wengenmayr, M.; Dockhorn, R.; Rabbell, H.; Knespel, M.; Checkervarty, A.; Sinapius, V.; Guo, H.; Werner, M. *LeMonADE-project/LeMonADE: LeMonADE v2.2.2*, 2021.
- (69) Müller, T.; Wengenmayr, M.; Dockhorn, R.; Knespel, M. *LeMonADE-project/LeMonADE-GPU*. Release v1.2, 2021.
- (70) Bunk, C.; Löser, L.; Fribicz, N.; Komber, H.; Jakisch, L.; Scholz, R.; Voit, B.; Seiffert, S.; Saalwächter, K.; Lang, M.; Böhme, F. Amphiphilic Model Networks Based on PEG and PCL Tetra-arm Star Polymers with Complementary Reactivity. *Macromolecules* **2022**, *55*, 6573–6589.
- (71) Horkay, F.; Hecht, A.-M.; Mallam, S.; Geissler, E.; Rennie, A. R. Macroscopic and Microscopic Thermodynamic Observations in Swollen Poly(vinyl acetate) Networks. *Macromolecules* **1991**, *24*, 2896–2902.
- (72) Ornstein, L. S.; Zernike, F. Accidental deviations of density and opalescence at the critical point of a single substance. *Proceedings of the Royal Netherlands Academy of Arts and Sciences* **1914**, *17*, 793–806.
- (73) Teixeira, J. Small-Angle Scattering by Fractal Systems. *J. Appl. Crystallogr.* **1988**, *21*, 781–785.
- (74) Debye, P.; Bueche, A. M. Scattering by an Inhomogeneous Solid. *J. Appl. Phys.* **1949**, *20*, 518–525.
- (75) Bierens de Haan, D. *Nouvelles Tables D'intégrales Définies*; P. Engels: Leiden, 1867. p Table 361.
- (76) Gradshteyn, I. S.; Ryzhik, I. M. *Table of Integrals, Series, and Products*; Jeffrey, A., Zwillinger, D., Eds.; Elsevier: Burlington, 2007. p Equation 3.944.5.
- (77) Freltoft, T.; Kjems, J. K.; Sinha, S. K. Power-law correlations and finite-size effects in silica particle aggregates studied by small-angle neutron scattering. *Phys. Rev. B* **1986**, *33*, 269–275.
- (78) Chen, S.-H.; Teixeira, J. Structure and Fractal Dimension of Protein-Detergent Complexes. *Phys. Rev. Lett.* **1986**, *57*, 2583–2586.
- (79) Falcao, A. N.; Pedersen, J. S.; Mortensen, K. Structure of Randomly Cross-Linked Poly(dimethylsiloxane) Networks Produced by Electron Irradiation. *Macromolecules* **1993**, *26*, 5350–5364.
- (80) Clisby, N. Accurate Estimate of the Critical Exponent ν for Self-Avoiding Walks via a Fast Implementation of the Pivot Algorithm. *Phys. Rev. Lett.* **2010**, *104*, 055702.
- (81) Shibayama, M.; Tanaka, T.; Han, C. C. Small angle neutron scattering study on poly(N-isopropyl acrylamide) gels near their volume-phase transition temperature. *J. Chem. Phys.* **1992**, *97*, 6829–6841.
- (82) Hammouda, B.; Ho, D. L.; Kline, S. Insight into Clustering in Poly(ethylene oxide) Solutions. *Macromolecules* **2004**, *37*, 6932–6937.
- (83) Strutt, J. W. On the scattering of light spherical shells, and by complete spheres of periodic structure, when the refractivity is small. *Proc. Royal Soc. London. Series A* **1918**, *94*, 296–300.
- (84) Pedersen, J. S. Analysis of small-angle scattering data from colloids and polymer solutions: modeling and least-squares fitting. *Adv. Colloid Interface Sci.* **1997**, *70*, 171–210.
- (85) Pusey, P. N.; van Megen, W. Dynamic light scattering by non-ergodic media. *Physica A* **1989**, *157*, 705–741.
- (86) Joosten, J. G. H.; McCarthy, J. L.; Pusey, P. N. Dynamic and Static Light Scattering by Aqueous Polyacrylamide Gels. *Macromolecules* **1991**, *24*, 6690–6699.
- (87) Mallam, S.; Hecht, A.; Geissler, E.; Pruvost, P. Structure of swollen polydimethyl siloxane gels. *J. Chem. Phys.* **1989**, *91*, 6447–6454.
- (88) Horkay, F.; Hecht, A.-M.; Zrinyi, M.; Geissler, E. Effect of Cross-links on the Structure of Polymer Gels. *Polym. Gels Networks* **1996**, *4*, 451–465.
- (89) Tsuji, Y.; Nakagawa, S.; Gupit, C. I.; Ohira, M.; Shibayama, M.; Li, X. Selective Doping of Positive and Negative Spatial Defects into Polymer Gels by Tuning the Pregel Packing Conditions of Star Polymers. *Macromolecules* **2020**, *53*, 7537–7545.
- (90) Narten, A. H.; Levy, H. A. Liquid Water: Molecular Correlation Functions from X-Ray Diffraction. *J. Chem. Phys.* **1971**, *55*, 2263–2269.
- (91) Skinner, L. B.; Huang, C.; Schlesinger, D.; Pettersson, L. G. M.; Nilsson, A.; Benmore, C. J. Benchmark oxygen-oxygen pair-distribution function of ambient water from X-ray diffraction measurements with a wide Q-range. *J. Chem. Phys.* **2013**, *138*, 074506.
- (92) Nishi, K.; Asai, H.; Fujii, K.; Han, Y.-S.; Kim, T.; Sakai, T.; Shibayama, M. Small-Angle Neutron Scattering Study on Defect-Controlled Polymer Networks. *Macromolecules* **2014**, *47*, 1801–1809.
- (93) Matsunaga, T.; Sakai, T.; Akagi, Y.; Chung, U.-I.; Shibayama, M. Structure Characterization of Tetra-PEG Gel by Small-Angle Neutron Scattering. *Macromolecules* **2009**, *42*, 1344–1351.
- (94) Benoit, H. On the effect of branching and polydispersity on the angular distribution of the light scattered by Gaussian coils. *J. Polym. Sci.* **1953**, *11*, 507–510.
- (95) Willner, L.; Jucknischke, O.; Richter, D.; Roovers, J.; Zhou, L.-L.; Toporowski, P. M.; Fetters, L. J.; Huang, J. S.; Lin, M. Y.; Hadjichristidis, N. Structural Investigation of Star Polymers in Solution by Small-Angle Neutron Scattering. *Macromolecules* **1994**, *27*, 3821–3829.

- (96) Daoud, M.; Cotton, J. P.; Farnoux, B.; Jannink, G.; Sarma, G.; Benoit, H.; Duplessix, C.; Picot, C.; de Gennes, P. G. Solutions of Flexible Polymers. Neutron Experiments and Interpretation. *Macromolecules* **1975**, *8*, 804–818.
- (97) Rubinstein, M.; Colby, R. *Polymer Physics*; OUP Oxford, 2003.
- (98) Brown, W.; Nicolai, T. Static and dynamic behavior of semidilute polymer solutions. *Colloid Polym. Sci.* **1990**, *268*, 977–990.
- (99) Hecht, A.-M.; Horkay, F.; Geissler, E.; Benoit, J. P. Small-Angle X-ray Scattering from Poly(vinyl acetate) Solutions and Networks Swollen in Acetone. *Macromolecules* **1991**, *24*, 4183–4187.
- (100) Geissler, E.; Hecht, A.-M.; Mallam, S.; Horkay, F.; Zrinyi, M. Neutron scattering and swelling properties of end-linked polydimethylsiloxane networks. *Makromol. Chem. Macromol. Symp.* **1990**, *40*, 101–108.
- (101) Mallam, S.; Horkay, F.; Hecht, A.-M.; Rennie, A. R.; Geissler, E. Microscopic and Macroscopic Thermodynamic Observations in Swollen Poly(dimethylsiloxane) Networks. *Macromolecules* **1991**, *24*, 543–548.
- (102) Matsunaga, T.; Sakai, T.; Akagi, Y.; Chung, U.-I.; Shibayama, M. SANS and SLS Studies on Tetra-Arm PEG Gels in As-Prepared and Swollen States. *Macromolecules* **2009**, *42*, 6245–6252.
- (103) Daoud, M.; Cotton, J. P. Star shaped polymers: a model for the conformation and its concentration dependence. *J. Phys. (Paris)* **1982**, *43*, 531–538.
- (104) Rubinstein, M.; Panyukov, S. Elasticity of polymer networks. *Macromolecules* **2002**, *35*, 6670–6686.
- (105) Lang, M. Monomer fluctuations and the distribution of residual bond orientations in polymer networks. *Macromolecules* **2013**, *46*, 9782–9797.
- (106) Lang, M. Relation between Cross-Link Fluctuations and Elasticity in Entangled Polymer Networks. *Macromolecules* **2017**, *50*, 2547–2555.
- (107) Hammouda, B. SANS from homogeneous polymer mixtures: A unified overview. *Adv. Polym. Sci.* **1993**, *106*, 87–133.
- (108) Panyukov, S.; Rabin, Y. Statistical physics of polymer gels. *Phys. Rep.* **1996**, *269*, 1–131.
- (109) Lang, M.; John, A.; Sommer, J.-U. Model simulations on network formation and swelling as obtained from cross-linking copolymerization reactions. *Polymer* **2016**, *82*, 138–155.
- (110) Takahashi, H.; Shibayama, M.; Fujisawa, H.; Nomura, S. Equilibrium Swelling and Small-Angle Neutron-Scattering Study on End-Linked Poly(tetrahydrofuran) Networks. *Macromolecules* **1995**, *28*, 8824–8828.
- (111) Obukhov, S. P.; Rubinstein, M.; Colby, R. H. Network modulus and superelasticity. *Macromolecules* **1994**, *27*, 3191–3198.
- (112) Horkay, F.; Hecht, A.-M.; Geissler, E. Fine Structure of Polymer Networks As Revealed by Solvent Swelling. *Macromolecules* **1998**, *31*, 8851–8856.
- (113) Rouf-George, C.; Munch, J. P.; Beinert, G.; Isel, F.; Pouchelon, A.; Palierne, J. F.; Boué, F.; Bastide, J. About "Defects" in Networks made by End-linking. *Polym. Gels Networks* **1996**, *4*, 435–450.
- (114) Urayama, K.; Kawamura, T.; Hirata, Y.; Kohjiya, S. SAXS study on poly(dimethylsiloxane) networks with controlled distributions of chain lengths between crosslinks. *Polymer* **1998**, *39*, 3827–3833.
- (115) Flory, P. J. Elastic Activity of Imperfect Networks. *Macromolecules* **1982**, *15*, 99–100.
- (116) Lang, M.; Kreitmeier, S.; Göritz, D. Trapped entanglements in polymer networks. *Rubber Chem. Technol.* **2007**, *80*, 873–894.
- (117) Bastide, J.; Leibler, L. Large-Scale Heterogeneities in Randomly Cross-Linked Networks. *Macromolecules* **1988**, *21*, 2647–2649.
- (118) Bastide, J.; Leibler, L.; Prost, J. Scattering by Deformed Swollen Gels: Butterfly Isointensity Patterns. *Macromolecules* **1990**, *23*, 1821–1825.
- (119) Rouf-George, C.; Munch, J.-P.; Schosseler, F.; Pouchelon, A.; Beinert, G.; Boué, F.; Bastide, J. Thermal and Quenched Fluctuations of Polymer Concentration in Poly(dimethylsiloxane) Gels. *Macromolecules* **1997**, *30*, 8344–8359.
- (120) Higgs, P. G.; Ball, R. C. Polydisperse polymer networks: elasticity, orientational properties, and small angle neutron scattering. *J. Phys. (Paris)* **1988**, *49*, 1785–1811.
- (121) Burchard, W. Solution Properties of Branched Macromolecules. *Adv. Polym. Sci.* **1999**, *143*, 113–194.
- (122) Norisuye, T.; Masui, N.; Kida, Y.; Ikuta, D.; Kokufuta, E.; Ito, S.; Panyukov, S.; Shibayama, M. Small angle neutron scattering studies on structural inhomogeneities in polymer gels: irradiation cross-linked gels vs. chemically cross-linked gels. *Polymer* **2002**, *43*, 5289–5297.
- (123) Toussaint, D.; Wilczek, F. Particle-antiparticle annihilation in diffusive motion. *J. Chem. Phys.* **1983**, *78*, 2642–2647.
- (124) Lang, M. Cyclic Structures in Polymer Model Networks. *Macromol. Symp.* **2019**, *385*, 1800168.
- (125) Lang, M.; Göritz, D.; Kreitmeier, S. The Effect of Spatially Inhomogeneous Mixing of Polymer and Cross-Links for End-Linked Polymer Networks. *Constitutive Models for Rubber III*, 2003; pp 195–202.
- (126) Kawamoto, K.; Zhong, M.; Wang, R.; Olsen, B. D.; Johnson, J. A. Loops versus Branch Functionality in Model Click Hydrogels. *Macromolecules* **2015**, *48*, 8980–8988.
- (127) Ikkai, F.; Shibayama, M. Inhomogeneity Control in Polymer Gels. *J. Polym. Sci. B* **2005**, *43*, 617–628.
- (128) Milner, S. T.; Witten, T. A.; Cates, M. E. A Parabolic Density Profile for Grafted Polymers. *Eur. Phys. Lett.* **1988**, *5*, 413–418.
- (129) Romeis, D.; Lang, M. Excluded volume effects in polymer brushes at moderate chain stretching. *J. Chem. Phys.* **2014**, *141*, 104902.
- (130) Norisuye, T.; Kida, Y.; Masui, N.; Tran-Cong-Miyata, Q.; Maekawa, Y.; Yoshida, M.; Shibayama, M. Studies on two Types of Built-in Inhomogeneities for Polymer Gels: Frozen Segmental Concentration Fluctuations and Spatial Distribution of Cross-Links. *Macromolecules* **2003**, *36*, 6202–6212.
- (131) Nie, J.; Du, B.; Oppermann, W. Influence of Formation Conditions on Spatial Inhomogeneities in Poly(N-isopropylacrylamide) Hydrogels. *Macromolecules* **2004**, *37*, 6558–6564.